

# Hydrodynamic Models for Heavy Ion Collisions\*

*P. Huovinen*

Department of Physics, University of Virginia, Charlottesville, VA 22904, USA

and

Helsinki Institute of Physics, FIN-00014 University of Helsinki, Finland

email: *ph4h@virginia.edu*

*P.V. Ruuskanen*

Department of Physics, FIN-40014 University of Jyväskylä, Finland

email: *vesa.ruuskanen@phys.jyu.fi*

KEYWORDS: hydrodynamics, quark-gluon plasma, elliptic flow, electromagnetic emission

**ABSTRACT:** Application of hydrodynamics for modeling of heavy-ion collisions is reviewed. We consider several physical observables that can be calculated in this approach and compare them to the experimental measurements.

## CONTENTS

INTRODUCTION . . . . .	2
HYDRODYNAMIC EXPANSION . . . . .	4
<i>Hydrodynamic Equations</i> . . . . .	4
<i>Initial Conditions</i> . . . . .	6
<i>The Equation of State of Strongly Interacting Matter</i> . . . . .	12
<i>Transverse flow</i> . . . . .	13
HADRON DISTRIBUTIONS AND CORRELATIONS . . . . .	14
<i>Freeze-out and the calculation of hadron spectra</i> . . . . .	14
<i>Transverse momentum spectra of hadrons</i> . . . . .	16
<i>Elliptic Flow</i> . . . . .	20
<i>Two-Particle Bose-Einstein Correlations</i> . . . . .	25
ELECTROMAGNETIC EMISSION . . . . .	28
<i>Photons at SPS</i> . . . . .	31
<i>Photons at RHIC</i> . . . . .	32
<i>Dilepton calculations</i> . . . . .	35
CONCLUDING REMARKS . . . . .	36

\*Final version of this review is scheduled to appear in the Annual Review of Nuclear

## 1 INTRODUCTION

Quantum chromodynamics (QCD), the theory on strong interactions, has been tested extensively in hard, large-momentum processes. In these processes, a large amount of energy or three-momentum is transferred to one (e.g., deep inelastic scattering) or few (jet production) quark and gluon constituents of initial hadrons. Owing to the asymptotic freedom property of QCD, the coupling strength is small. The time scale for this part is a small fraction of the time scale of the overall process. These two properties allow the factorization and perturbative treatment of the hard part of the process from the rest of the matrix element. This programme has been very successful, and no clear discrepancies have been found between experimental results and theoretical calculations.

The goal of the experimental heavy ion program at ultra-relativistic energies is to study QCD in an environment very different from that encountered in hard processes, in a dense system of quarks and gluons. When the heavy ion programme started two decades ago, the original goals were the production and study of dense, thermally equilibrated, strongly interacting matter, the quark-gluon plasma (QGP). Although this is still the highest priority, phenomena other than the formation of thermally equilibrated QGP also occur in dense partonic systems and can be studied in heavy ion collisions. E.g. the existence of what is called a Color Glass Condensate (CGC), which is related to the saturation of gluon occupation numbers in dense components of initial wave functions, may be important for the formation of the QGP and may also have other observable effects (1). Also, the phenomenon of jet quenching, the loss of energy of a high-energy parton (quark or gluon) when it traverses a high-density parton system, can be expected to occur in the dense environment of heavy ion collisions, even when the system is not fully equilibrated.

The earlier experiments at Brookhaven National Laboratory (BNL) and CERN-SPS provided clear evidence of collective phenomena in nuclear collisions. Recent results from experiments at the Relativistic Heavy Ion Collider (RHIC) at BNL show that total multiplicities exceeding 1000 particles per unit rapidity,  $dN/dy \gtrsim 1000$ , are produced in central (head-on) collisions of gold nuclei at center-of-mass energies up to  $\sqrt{s_{NN}} = 200$  GeV. Here  $\sqrt{s_{NN}}$  is the center-of-mass energy for a nucleon pair. The measured average transverse momentum is  $p_T \gtrsim 0.5$  GeV, indicating a total energy per unit rapidity interval of  $dE_T/dy \gtrsim 500$  GeV. At time  $\tau$  after the nuclei have passed through one another, the volume occupied by the produced quanta in a rapidity interval  $\Delta y$  is  $\Delta V = \tau \Delta y A_T$ , or  $\tau A_T = \tau \pi R_A^2$  for unit rapidity. At  $\tau = 1$  fm/c the above numbers imply (2) a particle density of  $\sim 10$  fm<sup>-3</sup> and an energy density of  $\sim 5$  GeVfm<sup>-3</sup>, well above different estimates and the results from lattice calculations of the energy density at which the phase transition from confined hadrons to unconfined quarks and gluons occur.

The subject of this review is the use of hydrodynamic modeling to describe and Particle Science Vol. 56, to be published in November 2006 by Annual Reviews, see “www.annualreviews.org”.

the expansion and dilution of matter produced in nuclear collisions. One motivation for this is to formulate a framework to study different observable quantities and correlations among them. Obviously hydrodynamics alone does not suffice because, first, at high energies, particle production can not be included and, second, only the properties of produced particles, not the hydrodynamic densities during the expansion, can be measured directly. Below we describe a possible dynamic scenario to calculate the production of initial matter. This provides the initial conditions for solving the hydrodynamic equations. Because the production dynamics is still not completely under control, sometimes it may be useful to use physically motivated parametrizations of initial conditions to study, for example, how the details of particle spectra depend on different features of initial conditions. The hydrodynamic description also needs another supplement. A link from hydrodynamical quantities to particle spectra is necessary at the end of expansion, when the particles become independent and fly to detectors.

The use of hydrodynamic concepts like temperature, pressure, and flow velocity cannot be strictly justified for matter formed in a heavy ion collision. Although the total number of particles produced is several thousand at RHIC and may be an order of magnitude more in the future ALICE experiments at the Large Hadron Collider (LHC) at CERN, they hardly form a macroscopic system in the proper thermodynamic sense. However, one can argue for partial equilibration and the formation of collective phenomena from the numbers given above. At initial particle densities of the order of  $5\text{--}10\text{ fm}^{-3}$ , and even with modest estimates of cross sections of the order of  $1\text{--}2\text{ mb}$ , mean free paths are  $\lesssim 1\text{ fm}$ , much below the nuclear size  $2R_A \gtrsim 10\text{ fm}$ . Therefore, frequent collisions occur and momentum is transferred from denser regions toward less dense regions. In describing the main consequences of these secondary collisions, concepts like temperature and pressure are useful.

Although the use of hydrodynamics may be justified for some features of nuclear collisions, that need not be the case for others. Defining energy density and pressure in the usual way in terms of the local momentum distribution, one obtains for pressure of massless particles  $P = \epsilon/3$  for any isotropic momentum distribution  $f(p)$ ,  $p = |\mathbf{p}| = E$ . In this case, describing the build-up of collective motion or flow using hydrodynamics with  $P = \epsilon/3$  as the equation of state (EoS) could be a reasonable approach, even when the form of  $p$  dependence of  $f(p)$  differs from that of the thermal equilibrium distribution,  $f_{\text{th}}(p)$ . However, if  $f(p)$  differs significantly from  $f_{\text{th}}(p)$ , any conclusions based on the detailed momentum dependence of  $f(p)$  would fail. This could well be the case at large momenta. Initial production is expected to contain a component that has an approximate power-law behavior at large momenta. It will take longer and requires a larger volume than available to change this power behavior to the exponential form of thermal distribution. The observed behavior of high- $p_T$  hadron spectra shows clearly that the high-momentum partons are not thermalized and that they suffer an energy loss while traversing the produced dense matter. Because the high-energy partons form only a small part of produced matter both in multiplicity and in transverse energy, a thermal equilibrium description can still be adequate

for the bulk of the matter.

Keeping in mind all the reservations, we review the use of hydrodynamics in describing the heavy ion collisions at collider energies, and the calculation of observable quantities. We compare the calculated results to the measurements mainly at RHIC, mentioning some results from the CERN-SPS. We also present examples of predictions for the future ALICE experiment at CERN.

## 2 HYDRODYNAMIC EXPANSION

Hydrodynamics is the theoretical framework describing the motion of fluid, a continuous, flowing medium. The equation of motion can be derived from kinetic equations. Hydrodynamic equations take the simplest form if local thermal equilibrium is assumed. In this treatment, there are no dissipative effects. To take such effects into account by approximation, small deviations from the local equilibrium are assumed. A linear treatment of deviations leads to a system of equations which contains the viscous coefficients including heat conductivity, in the case of conserved currents. For a review, see Reference (3). In most applications of hydrodynamics to heavy ion collisions, viscosity has been neglected. In studies with viscosity, results on global, integrated quantities do not differ qualitatively from those without viscosity. However, for example, transverse spectra at larger transverse momenta  $p_T \gtrsim 1.5$  GeV may start to deviate clearly from ideal-fluid calculation (4–6). One should remember, though, that the viscous properties of strongly interacting matter are not well understood, and the approximations in the numerical work also introduce uncertainties.

Once EoS is known and initial conditions are specified, the hydrodynamic equations determine the expansion of the fluid. In the context of describing heavy ion collisions, the use of these equations requires knowing the EoS of strongly interacting matter and the primary production of particles. Detailed knowledge of microscopic processes is not required if a very strong assumption is taken: The expanding system stays in local thermodynamical equilibrium. This becomes of great practical importance if one wants to include in the hydrodynamic expansion the transition from quarks and gluons to hadrons. The complicated deconfinement or hadronization processes need not be known in microscopic detail; all that is necessary is the thermodynamic equation of state as computed, for example, in lattice QCD.

### 2.1 Hydrodynamic Equations

The hydrodynamic equations

$$\partial_\mu T^{\mu\nu} = 0, \quad T^{\mu\nu} = (\epsilon + P)u^\mu u^\nu - P g^{\mu\nu} \quad (1)$$

express, in terms of the energy-momentum tensor  $T^{\mu\nu}$ , the conservation of energy and momentum in continuous, flowing matter. The quantities defining  $T^{\mu\nu}$  are:  $\epsilon :=$  the energy density,  $P :=$  the pressure, and  $u^\mu :=$  the flow four-velocity, normalized to  $u_\mu u^\mu = 1$  as usual. The simple form of  $T^{\mu\nu}$  above holds for an ideal fluid.

In addition, if the system contains conserved densities  $n_i$ , such as those of charge and baryon number, their evolution is expressed by continuity equations

$$\partial_\mu j_i^\mu = 0. \quad (2)$$

With several conserved densities or non-zero viscous terms, the definition of  $u^\mu$  is not unique. One can define the velocity in terms of one of the conserved currents by writing  $j_i^\mu = n_i u_i^\mu$ , where  $n_i = \sqrt{j_{i\mu} j_i^\mu}$ , or one can use the energy-momentum tensor to define the flow velocity. In the first case, usually referred to as the Eckart definition, there is no flow of charge  $Q_i$  in the local rest frame  $u_i^\mu = (1, 0)$ , the Eckart frame. For a non-ideal fluid, the energy flow would usually be non-zero in the Eckart frame. A definition of the fluid velocity in terms of the energy-momentum tensor, referred to as the Landau definition, is such that the energy flow is zero in the local rest frame, but usually the flow of different charges does not vanish. Here, the only charge we consider is the baryon density. We also treat the matter in the final state as an ideal fluid, and thus the two choices for the flow velocity coincide. For a review, see Reference (3).

The only properties of the dynamics contained in Equations 1 and 2 are the conservation laws. However, the relations between the thermodynamic densities  $\epsilon$ ,  $P$  and  $n_i$ , or alternatively their definitions in terms of temperature  $T$  and chemical potentials  $\mu_i$  — e.g.,  $\epsilon = \epsilon(T, \mu_i)$  — constituting the EoS, depend on the details of the dynamics among the constituents of the matter. The need for an EoS is obvious: The Equations 1 and 2 contain five equations whereas there are six quantities to be defined by solving the equations. These quantities are the three components of the velocity, the energy density, pressure and the baryon-number density. For a non-ideal flow, transport coefficients would enter into the expressions of the energy-momentum tensor and currents, and their derivation from theory requires the knowledge of microscopic dynamics in the same way as the derivation of EoS.

Most of the detailed hydrodynamical discussion below is limited to the situation of scaling longitudinal flow and invariance under longitudinal Lorentz boosts. This means that the longitudinal flow velocity is  $v_z = z/t$ , and hence, the flow rapidity is  $\eta = \log[(t+z)/(t-z)]$ , which is also often termed the space-time rapidity. If the initial densities are assumed to depend on  $t$  and  $z$  only through the longitudinal proper time  $\tau = \sqrt{t^2 - z^2}$ , e.g.,  $\epsilon = \epsilon(\tau, r)$ , the expansion will evolve so that densities remain independent of  $\eta$  and the  $v_z$  will retain the scaling form  $v_z = z/t$ . In this situation the system is said to be boost-invariant (2).

Before discussing the EoS in more detail, we note that the most useful form of the EoS for solving the hydrodynamical equations is provided by the relations among the densities  $\epsilon$ ,  $P$ , and  $n_i$  when the hydrodynamical equations are written in the form of Equations 1 and 2. In this form, temperature and chemical potentials do not appear in the equations. For the calculation of observable quantities, such as hadron spectra or electromagnetic emission, relations among the above densities and the temperature and chemical potentials must be specified, as we discuss below.

The other ingredient that must be provided from outside into the hydrodynamic

description are the initial conditions, e.g., in terms of initial energy distribution and velocity. From the physics point of view this is a very profound problem because it involves not only the primary production dynamics, but also the question of thermalization of produced particles. We discuss first the initial conditions, then the EoS, and finally the calculation of physical observables.

## 2.2 Initial Conditions

As mentioned above, primary particle production cannot be formulated within the hydrodynamic framework in a realistic way in high-energy nuclear collisions. The dynamics of particle production is a separate problem and, if solved, it provides the initial conditions for the hydrodynamic expansion. Initial conditions specify the thermodynamic state of the matter and its velocity on an appropriate space-time boundary, which, for example, in the boost-invariant case discussed below, can be taken to be a constant, longitudinal proper time surface  $\tau = \sqrt{t^2 - z^2} = \tau_0$ . From the point of view of the hydrodynamical calculation, the initial conditions can be provided either by a dynamical calculation of primary particle production or by a reasonable parametrization, with the parameters either given by physical arguments or fixed by comparing (some of) the results with experimental data.

There are different approaches to primary production, such as pQCD + final-state saturation (minijet) (7) and the color glass condensate model (8) based on the initial state parton saturation (9). Both describe the produced matter as a parton system. Also, models based on string formation and decay, such as the DPMJET model (10), are used for the calculation of final hadron spectra. In such a model, a varying fraction of energy is in the form of color strings at an early stage of the collision, and they are not readily connected with a hydrodynamic description that assumes particle-like constituents of matter. We do not consider string models further, but we describe briefly parton-based approaches to the primary production.

To illustrate different key factors that enter the determination of initial conditions from dynamical calculation of particle production, we consider a perturbative QCD calculation of parton production as an example. For such a calculation to converge, a cut-off must be provided on small momentum-transfer collisions. In this model the cut-off is obtained from a saturation condition expressed in terms of the transverse nuclear geometry and the number of produced partons. At collider energies, the saturation scale turns out to be typically  $p_{\text{sat}} \sim 1 \dots 3$  GeV, which is clearly larger than  $\Lambda_{\text{QCD}} \sim 0.2$  GeV. Because this cut-off is smaller than what is usually used in jet calculations, produced partons are often called minijets, as partons close to the cut-off dominate the production. In addition to the cut-off, the ingredients of the calculation are the parton distribution functions of colliding nuclei and the parton-parton cross sections. These cross sections can be calculated from basic QCD theory, but parton distributions must be provided from other measurements.

The nuclear parton distributions are usually expressed in terms of parton distributions of nucleons that, however, are known to be modified in nuclei. The

nuclear modification factor  $R_A(x, Q^2)$  is the nuclear parton distribution normalized to a single nucleon and divided by the parton distribution of a free nucleon.<sup>1</sup>

The perturbative QCD calculation of minijet production is a momentum-space calculation, as is the case in most production models. To define the initial spatial densities, a connection between the momentum of a produced parton and its space-time formation point is needed. At collider energies, the hard partons of the colliding nuclei are Lorentz contracted to a region on order of  $2R_A/\gamma_{\text{cm}} \ll 1$  fm. We consider the collision region as a point in the longitudinal direction that allows us to assume that the rapidity of the minijet coincides with the space-time rapidity of the formation point,  $y = \eta = (1/2) \ln[(t+z)/(t-z)]$ . We take the formation (proper) time to be the inverse of the saturation scale,  $\tau_0 = 1/p_{\text{sat}}$ . Thus, the minijet matter forms along the hyperbola  $t = \sqrt{z^2 + \tau_0^2}$  with initial longitudinal flow velocity  $v_z(\tau_0) = z/t$ . To determine the transverse distribution, we must start with a calculation of production cross section.

To obtain the initial conditions for baryon-number density and energy density, we first need the minijet cross sections for (anti)quarks and gluons and their first moments in transverse energy (momentum) in nucleon-nucleon collision, each calculated in a rapidity interval  $\Delta y$  and integrated in  $p_T$  from the saturation cut-off  $p_T = p_{\text{sat}}$  to its maximum value (11, 12):

$$\begin{aligned} \sigma_{\text{jet}}(p_{\text{sat}}, \sqrt{s}, \Delta y, A) &= \int_{p_{\text{sat}}}^{\sqrt{s}/2} dp_T \frac{d\sigma_{\text{jet}}(\sqrt{s}, \Delta y, A)}{dp_T}, \\ \sigma_{\text{jet}}\langle E_T \rangle(p_{\text{sat}}, \sqrt{s}, \Delta y, A) &= \int_{p_{\text{sat}}}^{\sqrt{s}/2} dp_T p_T \frac{d\sigma_{\text{jet}}(\sqrt{s}, \Delta y, A)}{dp_T}. \end{aligned}$$

The total number of minijets and the total amount of transverse energy in  $\Delta y$  in a nucleus-nucleus collision is obtained by multiplying the corresponding nucleon-nucleon cross section with the nucleon-nucleon luminosity of the collision (including an extra factor of two for the number of minijets). This is given by the overlap function  $T_{AB}(b)$  of transverse densities  $T_{A(B)}(s)$  of the colliding nuclei:

$$\begin{aligned} T_{AB}(\mathbf{b}) &= \int d^2\mathbf{s} T_A(|\mathbf{b} - \mathbf{s}|) T_B(s) = T_{AB}(b), \\ T_A(\mathbf{s}) &= \int_{-\infty}^{+\infty} dz \rho_A(z, \mathbf{s}) = T_A(s), \end{aligned}$$

where  $\mathbf{b}$  is the impact parameter and  $\mathbf{s}$  the transverse coordinate in nucleus  $A$ . For example the number of partons (which can be defined only in lowest order because it is not an infrared-safe quantity at higher orders) produced in a central zero-impact-parameter collision of equal nuclei is

$$\Delta N_{AA} = T_{AA}(0) \sigma_{\text{jet}}(p_{\text{sat}}, \sqrt{s}, \Delta y, A) \quad (3)$$

in a rapidity interval  $\Delta y$ . A similar expression with  $\sigma_{\text{jet}}$  replaced by  $\sigma_{\text{jet}}\langle E_T \rangle$  gives  $\Delta E_T$ , the transverse energy of minijets, in  $\Delta y$ .

Before discussing how to formulate the saturation condition to fix  $p_{\text{sat}}$ , we notice that the average densities are obtained by dividing the total quantity with the

<sup>1</sup>In the actual calculation protons and neutrons are treated separately.

volume that corresponds to the rapidity interval  $\Delta y$ ,  $\Delta V = \Delta z A_T = \tau_0 \Delta y \pi R_A^2$ . This procedure, with densities averaged over the transverse plane, is easily generalized to local densities. The nucleon–nucleon luminosity in a transverse-area element  $d^2\mathbf{s}$  is  $T_A(|\mathbf{b} - \mathbf{s}|)T_B(s)d^2\mathbf{s}$ , and the volume element is  $dV = \Delta z d^2\mathbf{s} = \tau \Delta y d^2\mathbf{s}$ , leading to (13)

$$n_{\text{pQCD}}(\tau_0, \mathbf{s}) = \frac{dN}{\tau_0 \Delta y d^2\mathbf{s}} = \frac{2\sigma_{\text{jet}}}{\tau_0 \Delta y} T_A(|\mathbf{b} - \mathbf{s}|) T_B(s) \quad (4)$$

for the parton density and

$$\epsilon_{\text{pQCD}}(\tau_0, \mathbf{s}) = \frac{dE_T}{\tau_0 \Delta y d^2\mathbf{s}} = \frac{\sigma_{\text{jet}} \langle E_T \rangle}{\tau_0 \Delta y} T_A(|\mathbf{b} - \mathbf{s}|) T_B(s) \quad (5)$$

for the energy density. The densities depend on the cut-off scale through the cut-off dependence of cross sections.

The minijet cross sections above can be calculated separately for gluon, quark, and anti-quark jets, allowing for the separate determination of the densities of quarks and anti-quarks. From these densities the initial net baryon number density is obtained as  $n_B = (n_q - n_{\bar{q}})/3$ , which provides the initial condition for the net-baryon-number current that satisfies the conservation law (Equation 2).

Up to here, we have essentially discussed how to obtain from a boost-invariant momentum-space calculation of production cross sections,  $\sigma_{\text{jet}}$  and  $\sigma_{\text{jet}} \langle E_T \rangle$ , the local densities  $n_B$  and  $\epsilon$ . To close the calculation of minijet cross sections, the saturation momentum  $p_{\text{sat}}$  must be specified, and we do this by assuming that the parton (mainly gluon) production saturates when the wave functions of produced partons start to overlap.

In the transverse direction the scale of the wave functions is  $1/p_{\text{sat}}$ . The scale in the longitudinal direction is not as obvious, but we assume it is the same at the production time  $\tau_0 = 1/p_{\text{sat}}$ . At this time, the volume occupied by particles in the rapidity interval  $\Delta y$  equals  $\Delta V = \tau_0 \Delta y A_T$ . At saturation, dividing this volume with the volume occupied by one jet,  $V_{\text{jet}}$ , should equal the number of produced partons  $\Delta N_{AA}$  in the rapidity interval  $\Delta y$ . This leads to the condition

$$\frac{\Delta N_{AA}(p_{\text{sat}}, \sqrt{s}, \Delta y, A)}{\Delta y} \frac{\pi}{(p_{\text{sat}})^2} = A_T = \pi R_A^2. \quad (6)$$

To avoid introducing a rather arbitrary cut-off parametrization at the nuclear edges in transverse plane, we do not try to define the calculation of  $p_{\text{sat}}$  locally in the transverse plane. Instead, an effective value  $p_{\text{sat}}$ , obtained from Equation 6 above, is used. Solving  $p_{\text{sat}}$  from this equation completes the calculation of primary production in the pQCD+saturation model. The initial energy densities at  $1/p_{\text{sat}}$  at RHIC and LHC energies,  $\sqrt{s_{NN}} = 200$  and 5500 GeV, respectively, are shown in Figure 1.

The above formulation of calculating the initial densities is applied in a central rapidity bin  $|y| \leq \Delta y$ . In the pQCD calculation, particle production depends on the rapidity through the parton distributions of colliding nuclei. However, when we use the results as initial conditions for the hydrodynamic calculation, we assume that boost-invariance is a good approximation at  $y \approx 0$  and take the densities to give the boost-invariant initial conditions with no  $\eta$  dependence.

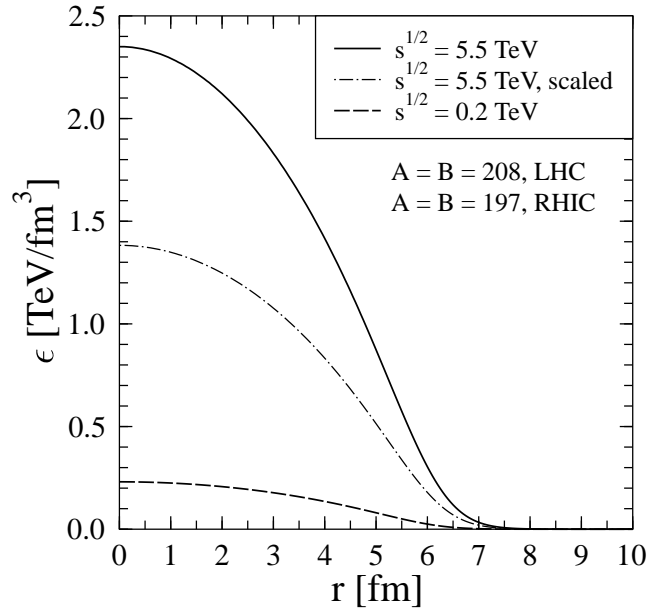


Figure 1: Transverse dependence of the initial energy distribution for a gold-on-gold collision at the Relativistic Heavy Ion Collider (RHIC) (dashed line) and lead-on-lead collision at the Large Hadron Collider (LHC) energy (solid line). The saturation scale is  $p_{\text{sat}} = 1.16$  GeV at RHIC and 2.03 GeV at the LHC, with formation times of 0.170 fm/c and 0.100 fm/c, respectively. The dashed-dotted line shows the energy density at the LHC if  $\tau_i = 0.170$  fm/c is used, emphasizing the strong dependence of initial energy density on the assumed initial time.

An attractive approach to particle production in heavy-ion collisions at collider energies has been based on the assumption that the initial-state parton densities saturate and non-linear dynamics becomes dominant (9). With increasing collision energy, the small- $x$  partons, in particular the gluons, become the dominant part in the production, and their density in the initial wave function of the nucleus becomes so high that gluons interact coherently and their density saturates. The momentum below which gluons saturate is called the saturation scale,  $Q_s$ . It depends on the collision energy  $\sqrt{s}$  and the mass number of the nuclei. From the point of view of the color fields, the high density or large occupation numbers of the field quanta with momenta  $\lesssim Q_s$  can be described as the formation of a color glass condensate. This part dominates the primary production at large  $\sqrt{s}$  and can be treated in terms of a classical effective field theory (1, 8). Quantum corrections to the classical treatment have also been considered ((14, 15); see also Reference (16) and references therein).

In the effective field theory approach to gluon production in  $AA$  collisions, when boost-invariance is assumed, a gauge can be chosen such that the problem can be formulated as a dimensionally reduced 2+1-dimensional theory. A numerical approach (17) with lattice regularization can be applied to the reduced theory.

The numerical calculations with lattice regularization started using SU(2) symmetry (18, 19) and other simplifications, such as cylindrical nuclei, but were soon

formulated for SU(3) (20, 21) and realistic nuclear geometry. Also, local color neutrality in the transverse overlap region of the collision (21) was imposed and other smaller inconsistencies corrected, leading to a ratio of  $E_T/N$ , which is consistent with the physical interpretation of the saturation scale (22).

The lattice approach does not, however, give a value of the saturation scale itself; the overall normalization must be obtained from elsewhere. For RHIC phenomenology, the authors of Reference (21) suggest two sets of results, which, in light of the latest results of Reference (22) lead to following, qualitatively different descriptions of the final state:

- In the case of a smaller scale  $\mu$ , the total transverse energy  $E_T \sim g_s^4 R_A^2 \mu^3$  produced from the classical fields roughly equals the experimentally measured result, whereas the number of initially produced partons ( $N \sim g_s^2 R_A^2 \mu^2$ ) is only about half of the multiplicity of hadrons measured in the experiment. In this case, the only change in the final state is the fragmentation of partons to  $\sim 2$  hadrons on average. However, there would be no significant hydrodynamic evolution because this would reduce the transverse energy below the measured value. In this picture, which corresponds to the scenario suggested by Kharzeev & Levin (23), one would expect the photon and lepton pair emission after the primary interactions to be very rare.
- For a larger saturation scale, the number of partons is close to the measured number of hadrons but the initially produced transverse energy is approximately 2.5 times bigger than the measured one (22). In this case, production must be followed by strong initial collective expansion in the longitudinal direction, allowing for a transfer of energy into the longitudinal motion. This case corresponds to the evolution suggested by pQCD + saturation + hydrodynamics calculation (13).

The energy dependence in the above models enters through the dependence of the saturation scales on the center-of-mass energy leading, for example, to rather similar growth of multiplicity from RHIC to the LHC in both models.

For a head-on, zero-impact-parameter collisions, the produced system is cylindrically symmetric, all quantities depend only on  $\tau$  and  $r$ , and the transverse flow is radial with no azimuthal dependence. We show results on hadron spectra displaying effects from radial flow. However, a good test for the applicability of the hydrodynamic description of heavy ion collisions is provided by nonzero-impact-parameter collisions without cylindrical symmetry. In our example of the calculation of primary densities the expressions (4, 5) hold also for nonzero-impact-parameter collisions. However, the determination of saturation scale becomes more involved, and a straightforward generalization of the saturation condition (Equation 6) leads the multiplicity to have a too-flat dependence on the number of participant nucleons, a possible measure of non-centrality of the collision (24).

Above, the transverse dependence of the initial densities is given by the number of collisions per unit transverse area:  $n_{\text{coll}}(\mathbf{b}, \mathbf{s}) \propto T_A(|\mathbf{b} - \mathbf{s}|)T_B(s)$ . In another popular phenomenological approach, the initial densities are assumed to

be proportional to the number of participants, also known as wounded nucleons<sup>2</sup> per unit transverse area. In the eikonal Glauber model, this is defined as

$$\begin{aligned} n_{\text{WN}}(\mathbf{s}; \mathbf{b}) &= T_A(\mathbf{s} + \frac{1}{2}\mathbf{b}) \left[ 1 - \left( 1 - \frac{\sigma T_B(\mathbf{s} - \frac{1}{2}\mathbf{b})}{B} \right)^B \right] \\ &+ T_B(\mathbf{s} - \frac{1}{2}\mathbf{b}) \left[ 1 - \left( 1 - \frac{\sigma T_A(\mathbf{s} + \frac{1}{2}\mathbf{b})}{A} \right)^A \right], \end{aligned} \quad (7)$$

where  $\sigma$  is the nucleon-nucleon cross section. For a zero-impact-parameter collision, this indicates, except at the edges of the nuclei, a radial dependence approximately proportional to the sum of thickness functions  $T_A(r)$  and  $T_B(r)$ . In the central region of the overlap area, the resulting density distribution is flatter than when the density is proportional to the number of collisions. This means smaller pressure gradients and slower evolution of transverse flow.

In the literature, both the proportionality to the number of binary collisions and to the number of participants has been used to fix either the initial entropy density or energy density. The proportionality constant is chosen to reproduce the measured final particle multiplicity in most central collisions. The centrality dependence of the multiplicity is then predicted by the model, but at RHIC, neither binary-collision scaling nor wounded-nucleon scaling reproduces the data. However, a linear combination of them does and is therefore used to describe the initial density distribution (25, 26).

We have not yet specified the initial transverse velocity  $\mathbf{v}_T$ . Usually this is taken to be zero. This choice is supported by the argument that the final state in each primary collision is randomly oriented in the transverse plane and thus one expects the transverse-momentum average in any volume element to vanish. There is a slight flaw in this argument because the transverse density of produced partons is not constant, and this can lead to a nonzero momentum average in a (finite) volume element. However, comparison to experimental data shows that for agreement, only small initial transverse velocities are allowed. In the calculations shown below,  $\mathbf{v}_T(\tau_0, \mathbf{r}) = 0$  has been used.

Because the use of hydrodynamics presumes thermal equilibrium, the time scale for thermalization after the primary production must be fixed. The dynamics of thermalization can be even more difficult to solve than that of primary production. Results of theoretical studies of thermalization have not yet converged. In the so-called bottom-up thermalization scenario (27), thermalization times are predicted to be long, of the order of 2...4 fm/c. A more recent idea of the role of instabilities in the expansion predicts much shorter thermalization times of order below 1 fm/c (28).

The thermalization time scale is an important issue because a hydrodynamic description of the elliptic flow can be achieved only if the thermalization time is short. In the numerical examples we provide below, we always use thermalization times below 1 fm/c. When showing results based on the minijet initial state, we use the production time scale as the thermalization time,  $\tau_i = 1/p_{\text{sat}}$ .

---

<sup>2</sup>Strictly speaking wounded nucleons are nucleons that scatter inelastically whereas participants are nucleons that scatter elastically or inelastically. In the recent literature this difference is usually ignored and both terms are used in the sense of participants.

### 2.3 *The Equation of State of Strongly Interacting Matter*

A major complication in the description of the evolution of the matter produced in a high-energy collision of nuclei is the change in the degrees of freedom. The dense initial-state parton matter expands and turns into a gas of hadrons and hadron resonances when dilute and cool enough. According to the present understanding, at large  $\mu_B$  and small or moderate  $T$ , there exist different correlated phases, such as the phase with color-flavor locking (29). Nearing smaller  $\mu_B$ , the transition between hadron resonance gas and QGP is believed to be of first order when  $\mu_B$  is not too small. For two light quarks and one heavy quark, the phase boundary is conjectured to end at a critical point, and below that the transition is a rapid cross-over. The quantitative theoretical information from QCD lattice simulations, which have recently been extended from the  $T$ -axis to finite chemical potential, supports this picture. There are also arguments in favor of the existence of strong correlations in the quark matter close to the phase boundary. These may explain the ideal-fluid behavior of QGP indicated by successful hydrodynamical explanation of elliptic flow. When matter is assumed to be in the state of non-interacting quarks and gluons, the ideal QGP, a simple ideal gas EoS of massless particles ( $P = \epsilon/3$ ) is often used to describe it. A more sophisticated but less usual way is to use parametrized lattice QCD results.

In heavy ion collisions at collider energies the net-baryon number is small, with  $\mu_B \lesssim 50$  MeV (30), indicating a cross-over transition. Somewhat unexpectedly, from the point of view of hydrodynamic expansion, the difference between a weak first-order transition and a rapid cross-over is not very significant, as long as the EoSs are relatively similar away from the transition region and the increase in entropy and energy densities around the critical temperature is sufficiently large and rapid (31). Upon a closer look this is not so surprising because the main qualitative feature is a jump in the thermodynamical densities  $\epsilon$  and  $s$ . The size of the jump depends essentially on the size of the change of the number of degrees of freedom. From the point of view of hydrodynamics, the rapid jump in  $\epsilon$  combined with a slower change in pressure appears as a softening of the EoS. It is seen as a slow-down in the acceleration of the transverse flow in the transition region. Details differ for the two cases, but the final features of flow are quite similar and the quantitative differences in the final hadron spectra are small.

An interacting hadron gas can be described in good approximation as a gas of noninteracting hadrons and resonances. The inclusion of resonances mimics the effects of both attractive and repulsive interactions between hadrons reasonably well (32). However, the repulsive interaction between baryons at large net-baryon densities must be included as an additional mean field (33) or as an excluded volume correction (34) to give a reasonable phase-transition behavior between hadronic and partonic phases. A detailed account of constructing an EoS with a mean field can be found, for example in Reference (35).

In calculations, we use an EoS with ideal QGP in the high-temperature phase and a hadron resonance gas with a mean field below the transition. A first-order transition is implemented by introducing a bag constant  $B$  into the QGP phase and connecting the two phases with a Maxwell construction. We use  $N_f = 3$ ,

and the bag constant  $B$  and mean field constant  $K$  are chosen to be  $B^{1/4} = 243$  MeV and  $K = 450$  MeV fm<sup>3</sup>, respectively, giving  $T_c = 167$  MeV for the transition temperature.

An additional complication in constructing an EoS of a hadron gas relevant for heavy ion collisions is the chemical composition of the hadron gas. The usual assumption of hydrodynamics is that of chemical equilibrium. This assumption is supported by thermal models that can reproduce the observed hadron abundances by assuming a thermal source in  $T \approx 170$  MeV temperature. However, many studies have found that the  $p_T$  distributions of hadrons are better described by assuming a colder, flowing source in  $T = 100$ – $140$  MeV temperature. Thus, the assumption of chemical equilibrium between these temperatures is questionable. In many hydrodynamical calculations, this observation is simply ignored and chemical equilibrium is assumed to hold until kinetic freeze-out at  $T = 100$ – $140$  MeV. In such cases one can reproduce the slopes of the hadron  $p_T$  spectra, but it is not possible to reproduce simultaneously both baryon and antibaryon yields.

One solution to this problem is the so-called single freeze-out model (36), in which a suitable choice of freeze-out surface allows one to fit the  $p_T$  spectra, even if the kinetic freeze-out temperature is taken to be the same  $T \approx 165$  MeV as the chemical freeze-out temperature. As we show below, in the context of hydrodynamical models, similar approach with  $T \approx 150$  MeV can be used to reproduce, at least approximately, the hadron  $p_T$  distributions in most central collisions at RHIC energies (37). Whether the anisotropies of particle distributions (see section 3.3) can also be reproduced this way, has not been tested so far.

Another solution to this problem is to assume two separate freeze-outs — chemical and kinetic — and to modify the EoS between these temperatures accordingly. In such an approach, the hadron yields are assumed to be fixed at some chemical freeze-out temperature, usually soon below or at the phase-transition temperature. These hadron yields are subsequently described as conserved currents, and each conserved hadron species is assigned a chemical potential. This way the yields of all hadron species can be reproduced separately, even if a low kinetic freeze-out temperature is used (38).

Such an EoS changes the buildup of collective motion — i.e. flow — very little because pressure as a function of energy density,  $P = P(\epsilon)$ , is very similar to the chemical equilibrium EoS (39, 40). However, temperature as a function of energy density changes radically, and when collective and thermal motion are folded to calculate observable particle distributions, the results differ (40, 41).

## 2.4 Transverse flow

To illustrate the transverse flow, Figure 2 shows the boundaries of QGP and hadron gas, with the mixed phase between them. Also, three contours of temperature are depicted, as well as the flow lines with 1-fm intervals starting at  $\tau_0$ . The initial conditions are those from the pQCD + saturation model at RHIC energy  $\sqrt{s_{NN}} = 200$  GeV.

According to this calculation, the maximum lifetime of the plasma phase is

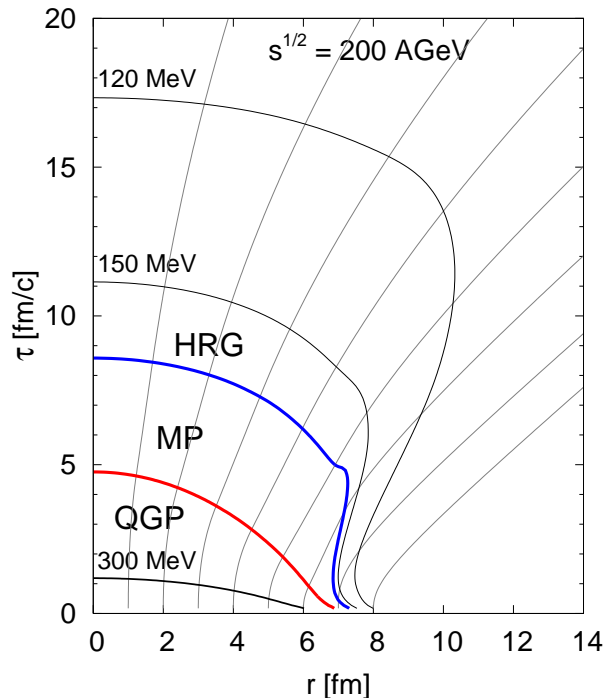


Figure 2: Temperature contours at 300 (in quark-gluon plasma QGP), 150 and 120 MeV (hadron resonance gas, HRG), and the boundaries of mixed phase (MP) with QGP and HRG at  $T_c = 167$  MeV. Flow lines are also shown. Initial conditions are from a pQCD + saturation calculation at  $\sqrt{s_{NN}} = 200$  GeV. Note that the slope of the flow line is related to the velocity and the curvature to the acceleration.

5 fm/c, and that of the mixed phase is  $\sim 8$  fm/c. The flow lines show how the fluid elements accelerate and move. The slope of the flow line is related to the velocity of the fluid and the curvature to the acceleration. In the mixed phase, where the pressure is constant, flow lines are straight because there is no acceleration. At small  $r$ , gradients are small and the flow lines bend slowly. In particular, in the plasma, when  $r$  increases, the pressure gradient, and consequently the acceleration, increases, indicated by the faster bending of flow lines. Along the flow line starting at  $r = 8$  fm/c, the densities are small even at  $\tau_0$ , and this region is insignificant in calculating the spectra. For calculational reasons the initial densities are taken to go smoothly to zero, and the hydrodynamic equations are also solved at large values of  $r$ .

### 3 HADRON DISTRIBUTIONS AND CORRELATIONS

#### 3.1 Freeze-out and the calculation of hadron spectra

As matter expands, distances between particles become large, collisions cease and momentum distributions freeze out. The condition for the freeze-out to occur is usually expressed locally in terms of the energy density or temperature reaching a given value. This determines a three-dimensional freeze-out surface  $\sigma^\mu(x)$  in

space-time. The prescription of Cooper and Frye (42) convolutes the flow with the thermal motion along the freeze-out surface:

$$\pi \frac{dN}{d^3\mathbf{p}/E} = \frac{dN}{dydp_T^2} = \pi \int_{\sigma} d\sigma_{\mu}(x) p^{\mu} f(x, p; T(x)) \quad (8)$$

$$= \frac{g}{2\pi} \sum_{n=1}^{\infty} (\pm 1)^{n+1} \int_{\sigma} r\tau \left[ -p_T I_1(n\gamma_r v_r \frac{p_T}{T}) K_0(n\gamma_r \frac{m_T}{T}) d\tau + m_T I_0(n\gamma_r v_r \frac{p_T}{T}) K_1(n\gamma_r \frac{m_T}{T}) dr \right]. \quad (9)$$

The second expression above is valid for cylindrically symmetric, boost-invariant flow with  $v_r$  the radial flow velocity,  $\gamma_r = 1/\sqrt{1-v_r^2}$ , and  $K_i$  and  $I_i$  are Bessel functions of second kind.

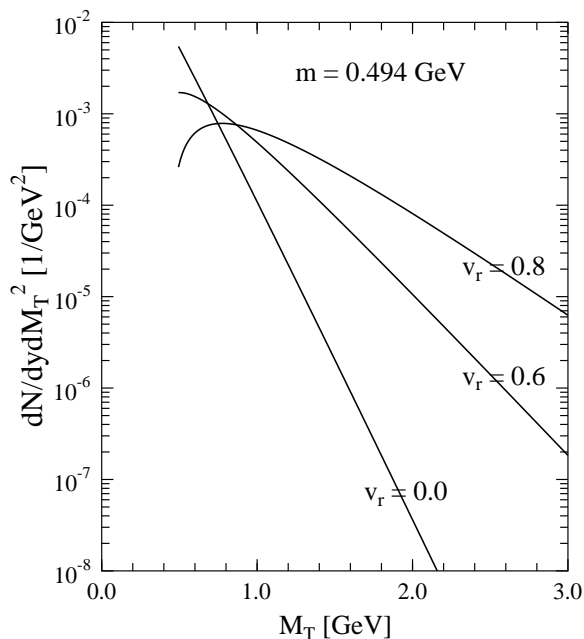


Figure 3: The effect of flow on the spectrum of kaons. Temperature is kept unchanged and the spectrum is shown for radially flowing matter at velocities  $v_r = 0, 0.6$  and  $0.8$ .

The unstable particles are treated as follows: First, the spectra of all hadrons and hadron resonances are calculated using Equation 9. We then follow the chains of all possible two- and three-body decays and collect the spectra of final stable hadrons (43). Stable hadrons can either be interpreted as all those that do not decay through strong interactions, or we can follow the feed-downs via weak and electromagnetic decays. E.g. we can calculate the  $\pi^0$  spectrum including both the  $\pi^0$ 's at freeze-out and all the decays that lead to  $\pi^0$ 's, and then study the photon spectrum from  $\pi^0$  decays alone or from all decays with photons in the final state. Phenomenologically an important case is that of feed-down nucleons from weak decays of strange hyperons. Here again, we can calculate, for example, the spectrum of  $\Lambda$ 's and then see how it contributes through weak decays to the spectrum of protons.

Before showing our results at RHIC and LHC energies we discuss how the radial flow affects a spectrum. In Figure 3 we show the spectrum of kaons from matter at rest or flowing at velocities  $v_r = 0.6$  and  $0.8$ . We assume that the matter decouples at a fixed time so that only the second term in Equation 9 contributes. The temperature of the matter is the same in each case and is essentially the inverse of the logarithmic slope of the spectrum for  $v_r = 0$ . From the asymptotic properties of modified Bessel functions of second kind, it is clear that at large  $m_T$  the change in the slope, when  $v_r$  changes to a nonzero value, can be expressed by replacing the temperature  $T$  with an effective temperature  $T_{\text{eff}} = T\sqrt{(1+v_r)/(1-v_r)}$ . For  $v_r = 0.6$  the change is a factor of two and for  $v_r = 0.8$  a factor of three.

### 3.2 Transverse momentum spectra of hadrons

Next we compare some of the hydrodynamical results (44) with the experimental transverse momentum spectra measured by the STAR (45–48), PHENIX (49–54), PHOBOS (55, 56) and BRAHMS (57–59) collaborations for the most central bins in Au+Au collisions at  $\sqrt{s_{NN}} = 130$  and 200 GeV. The calculated spectra are obtained by using Equation 9 with the flow illustrated in Figure 2.

Note that a hydrodynamic calculation cannot describe the hadron spectra at large transverse momenta. At large  $p_T$  the hydrodynamical calculation shows an approximate exponential behavior, whereas the tails of measured spectra essentially obey a power law. At RHIC, the transition from steep exponential to a shallower power behavior takes place at  $p_T \sim 3$  GeV. The fraction of hadrons with  $p_T \gtrsim 3$  GeV from all hadrons is small, and they originate from the fragmentation of high-energy partons, which suffer some energy loss in the dense medium of low-energy partons, but are not thermalized. We return to the interplay of the low-energy partons, which provide the main transverse energy and are assumed to thermalize, and the high-energy partons, which lose some fraction of energy in rescattering but require a much larger system for thermalization.

We start with the  $p_T$  spectra of identified hadrons at midrapidities. Figure 4 shows the PHENIX data collected for positive pions, kaons and protons in the most central 5 % of Au+Au collisions for  $y = 0$  at  $\sqrt{s_{NN}} = 130$  GeV (51). Similarly, in Figure 5 STAR (47), PHENIX (53) and BRAHMS (58, 59) data are shown at  $\sqrt{s_{NN}} = 200$  GeV. Note the scaling factors 10 and 1000 for kaons and protons, respectively. An important issue of uncertainty in the calculation is the dependence of the results on the decoupling temperature. This is shown by plotting the results for freeze-out temperatures  $T_{\text{dec}} = 150$  MeV (solid lines) and 120 MeV (dotted lines). Note that the normalization of the pion spectrum is almost independent of the decoupling temperature. Because pions provide the main contribution to the total multiplicity,  $dN_{\text{tot}}/dy$  depends only weakly on  $T_{\text{dec}}$ . However, the multiplicity of heavier particles is very sensitive to  $T_{\text{dec}}$ , as expected. The shape of all three spectra changes clearly with the decoupling temperature. This follows from the increase in flow velocity, characterized by the increase of the effect with the increasing mass of the particle. The aim of this calculation has not been to find a best fit to the data, but the results show that

both the normalization and the slope of the data at momenta  $p_T \lesssim 3$  GeV can be described quite well with a single  $T_{\text{dec}}$  in the neighborhood of 150 MeV.

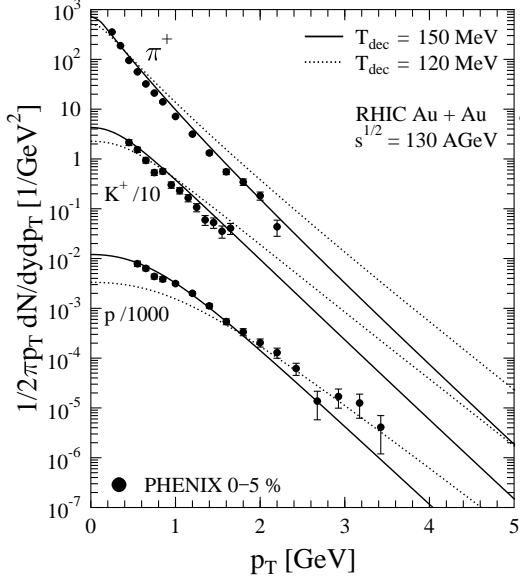


Figure 4: Transverse momentum spectra of positive pions, positive kaons, and protons at  $y = 0$  in the most central 5% of Au+Au collisions at  $\sqrt{s_{NN}} = 130$  GeV. The solid and dotted lines show our hydrodynamic results for freeze-out temperatures  $T_{\text{dec}} = 150$  MeV and  $T_{\text{dec}} = 120$  MeV, respectively. The PHENIX data (51) is plotted with the given total error bars. Note the scaling factors 10 and 1000 for kaons and protons, respectively. Both the hydrodynamic result and the PHENIX data contain the feed-down contributions from hyperons.

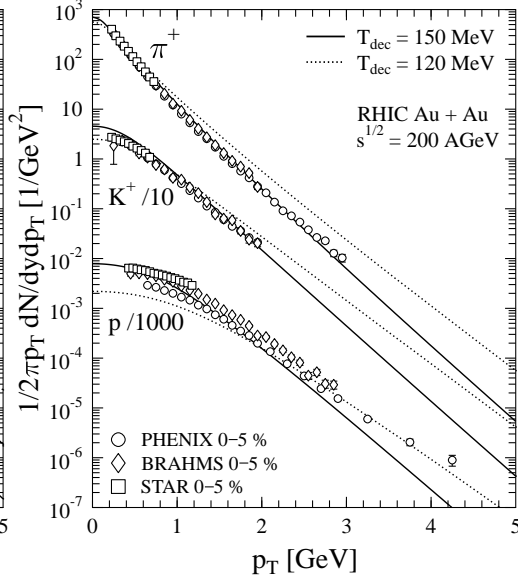


Figure 5: As Figure 4 but at  $\sqrt{s_{NN}} = 200$  GeV. The PHENIX data (53) and the BRAHMS data (58, 59) are shown with statistical errors and the STAR data (47) with the given total error bars. The hydrodynamic calculation and the PHENIX data are without the hyperon feed-down contributions whereas the STAR and BRAHMS data contain the feed-down.

For the identified particles in Figures 4 and 5, the measured spectra do not extend to large enough  $p_T$  to show clearly the deviation from the hydrodynamic results, with the exception of proton spectra. If the decoupling temperature is 150 MeV to reproduce the normalization, the slope tends to be too steep. The proton yield from jet fragmentation, as explained in detail in Reference (44), does not seem to be large enough in the  $p_T \sim 3 \dots 5$  GeV region to bring the calculation into agreement with the data. In Figure 6, the spectra of two other heavy particles are shown, those of antilambdas and antiprotons. These show the same trend as protons, pointing to the need for separate chemical and kinetic decoupling when describing simultaneously the details of all spectra. Studies with separate chemical and kinetic decoupling, in which the stable particle numbers are fixed after chemical freeze-out, indeed show that the spectra of pions and kaons become almost independent of the kinetic decoupling temperature  $T_{\text{dec,kin}}$ , whereas the

(anti)proton spectra widen with decreasing  $T_{\text{dec,kin}}$  (40, 41). There are, however, claims in the literature that separate chemical and kinetic decoupling lead to a worse overall fit to the slopes of  $p_T$  distributions than what can be achieved by requiring chemical equilibrium until kinetic freeze-out (60, 61). Studies exploring the effects of initial time, the shape of initial distributions, and the value of  $T_{\text{dec,chem}}$  while using two separate freeze-outs are needed to settle the issue.

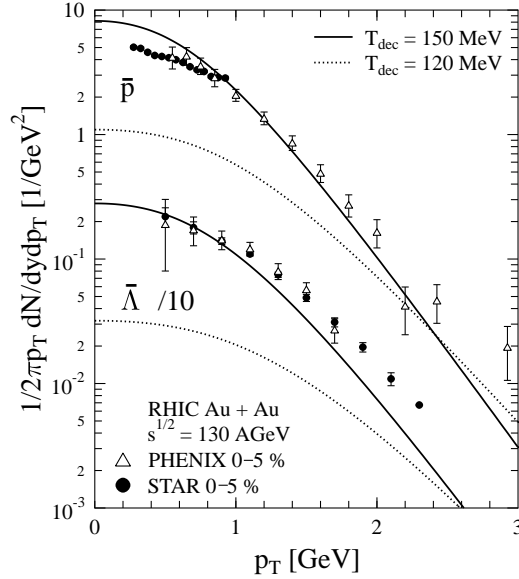


Figure 6: Transverse momentum spectra of antiprotons and antilambdas at  $y = 0$  in the most central 5 % of Au+Au collisions at  $\sqrt{s_{NN}} = 130$  GeV. Our hydrodynamic results are for freeze-out temperatures  $T_{\text{dec}} = 150$  MeV (solid line) and  $T_{\text{dec}} = 120$  MeV (dotted line), with hyperon feed-down contributions included, as in the PHENIX  $\bar{p}$  (51) and  $\bar{\Lambda}$  (52) data and the STAR data (48).

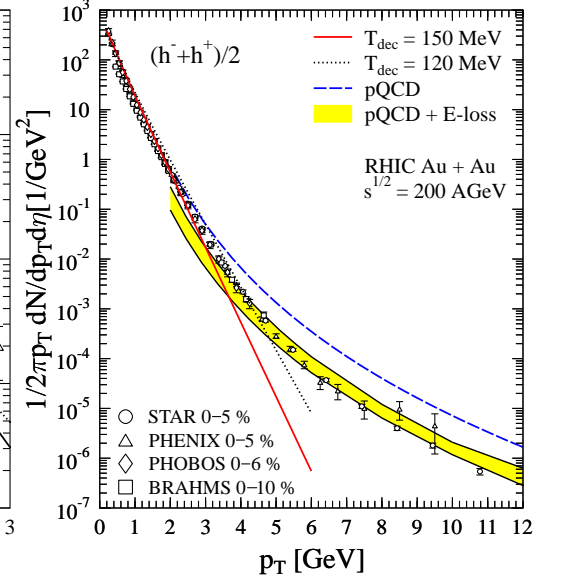


Figure 7: Transverse momentum spectra of charged particles at  $\eta = 0$  (averaged over  $|\eta| \leq 0.1$ ) in the most central 5 % of Au+Au collisions at  $\sqrt{s_{NN}} = 200$  GeV. Our hydrodynamic results are shown for  $T_{\text{dec}} = 150$  MeV (solid line) and  $T_{\text{dec}} = 120$  MeV (dotted line). The pQCD fragmentation results are shown with (shaded band) and without (dashed line, see the text) energy losses. The data is taken by STAR (45), PHENIX (49), PHOBOS (55), and BRAHMS (57).

The range where hydrodynamics can be used to describe the hadron spectra is indicated clearly in Figure 7, which shows results from our hydrodynamical calculations and from a pQCD jet calculation, followed by an energy loss in the medium before the jet fragments into hadrons (see below). The STAR and PHOBOS data are plotted with the given total error bars, the PHENIX data by adding the given statistical and systematic errors in quadrature, and the BRAHMS data with the given statistical error bars.

The transverse spectrum up to  $\sim 3$  GeV is similar to that of the dominant pion component shown separately in Figure 5. It has the shape typical of the spectrum from hydrodynamic calculations, falling off roughly exponentially. In the region

$p_T \sim 3 \dots 4$  GeV, there is a large change in the slope, indicating a change in the overall production mechanism. The calculation of primary production proceeds through the hard and semihard interactions between the partons of the incoming nuclei, both in the case of initial conditions for hydrodynamical equations and the energy loss of the jets. In the hydrodynamic calculation, the produced partons are assumed to thermalize quickly and then undergo hydrodynamic expansion in local thermal equilibrium until the freeze-out. In the calculation of jet fragmentation after energy loss, the produced high-energy partons are assumed to survive the thermalization, but lose energy when traversing the thermal medium formed by the lower-energy partons. When energy loss and fragmentation are taken into account, the original energy of the partons that fragment to hadrons of  $p_T \gtrsim 3$  GeV must be of the order of  $\sim 6$  GeV or greater. It turns out that the contribution of partons with  $p_T \gtrsim 4$  GeV to the production of (transverse) energy is less than 5 %, justifying as a good approximation the assumption that all produced transverse energy is thermalized. The details of the jet-energy-loss and fragmentation calculation are explained in References (44) and (62).

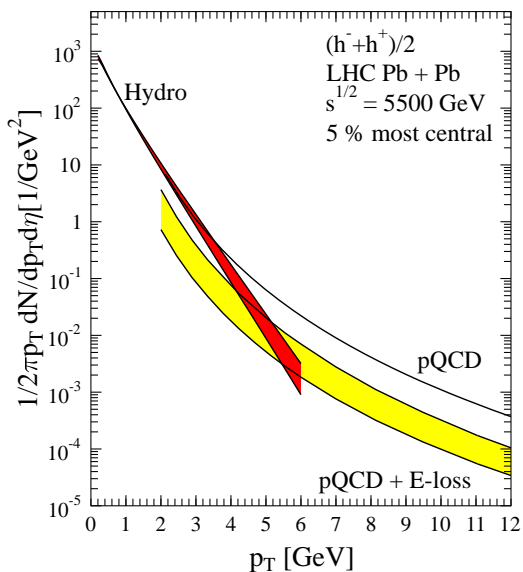


Figure 8: Predictions for the transverse momentum spectra of charged hadrons at  $\eta = 0$  in the most central 5 % of Pb+Pb collisions at Large Hadron Collider (LHC) energy  $\sqrt{s_{NN}} = 5500$  GeV. The shaded band in the hydrodynamic results shows the freeze-out temperature interval 120...150 MeV. The solid curve labeled "pQCD" corresponds to the pQCD fragmentation results without energy losses. The shaded band labeled "pQCD + E-loss" describes the uncertainty in the pQCD fragmentation results with energy losses.

Although the two-component approach, hydrodynamically expanding thermal matter as the source of low- $p_T$  hadrons and jet fragmentation after energy loss producing the high- $p_T$  hadrons, seems reasonable and justified, adding them straightforwardly would be too naive. In the region of turn-over from one mechanism to the other, both contribute, but part of the hadrons cannot be assigned to either component. Other mechanisms like recombination can also contribute

in this region (63). Accurate data in this area would be useful in understanding both the energy loss and thermalization of produced partons.

As an example of the dependence on the collision energy,  $\sqrt{s_{NN}}$ , Figure 8 shows an extension of the calculation to the CERN LHC, with  $\sqrt{s_{NN}} = 5500$  GeV for the heavy ion collisions. In the calculation of initial conditions from the primary parton interactions, all parameters are fixed except for the collision energy. The saturation scale changes from  $p_{\text{sat}} = 1.16$  GeV at RHIC energy to  $p_{\text{sat}} = 2.03$  GeV at the LHC. The total multiplicity increases from  $dN_{\text{tot}}/dy \approx 1000$  at RHIC to 4500 at the LHC. The initial thermal densities are higher and lead to longer expansion and stronger transverse flow at the decoupling. This is seen in the change of the region where the component of thermal particles goes over to the component of particles from jet fragmentation with energy loss. At RHIC the transition is centered around  $p_T \sim 3$  GeV, whereas at the LHC it is predicted to be  $p_T \sim 5$  GeV. The larger  $p_T$  region where thermal particles dominate should also be seen in elliptic flow. At the present RHIC energies, the hydrodynamic predictions of elliptic flow start to overshoot the data above  $p_T \sim 2$  GeV, but if the thermal component grows as predicted in Figure 8, the elliptic flow parameter  $v_2$  should follow the hydrodynamical calculation to larger transverse momenta.

### 3.3 Elliptic Flow

The particle production in primary collisions is azimuthally isotropic, whereas the reaction zone in noncentral collisions is not, but has an elongated shape. If produced particles rescatter, the particles moving in the direction of the longer axis of the reaction zone are more likely to change their direction than the particles moving in the direction of the shorter axis. Therefore the observed emission pattern of particles will be azimuthally anisotropic, and the more frequent the rescattering, the more anisotropic the particle distribution.

In this way, the anisotropy of the final particle distribution is a measurement of the frequency of rescatterings during the dense phase of the collision. This anisotropy can be quantified as the coefficients of the Fourier expansion of the azimuthal particle distribution (64):

$$\begin{aligned} \frac{dN}{dyd\phi_p} &= \frac{dN}{2\pi dy} (1 + 2v_1 \cos(\phi - \phi_R) + 2v_2 \cos 2(\phi - \phi_R) + \dots), \\ \frac{dN}{dydp_T d\phi_p} &= \frac{dN}{2\pi dy dp_T} (1 + 2v_1(p_T) \cos(\phi - \phi_R) \\ &\quad + 2v_2(p_T) \cos 2(\phi - \phi_R) + \dots), \end{aligned} \quad (10)$$

where  $\phi_R$  is the azimuthal angle of the event plane (the plane spanned by the beam direction and the impact parameter). Assuming that the experimental uncertainties in event-plane reconstruction can be corrected for, each event can be rotated such that  $\phi_R = 0$ . The first and second coefficient of the expansion,  $v_1$  and  $v_2$ , are usually referred to as directed and elliptic flow, respectively. Because the system is usually thinner in the direction parallel to the impact parameter, the in-plane direction, than in the out-of-plane direction, the value of  $v_2$  is positive.

At midrapidity, all uneven coefficients are zero owing to symmetry. At SPS and RHIC energies, the directed flow,  $v_1$ , is expected to be very small and most of the experimental and theoretical interest has been directed toward measuring and analyzing the elliptic flow,  $v_2$ . Recently the higher harmonics,  $v_4, v_6$  and  $v_8$ , have also been measured (65–67).

In a hydrodynamic picture, the buildup of momentum anisotropies is easy to understand in terms of pressure gradients. The average pressure gradient between the center of the system and the surrounding vacuum is larger in the direction where the collision system is thinner. Therefore, the collective flow is stronger in that direction and more particles are emitted there than in the orthogonal direction, where the collision system is longer.

As mentioned above, the more the particles rescatter, the larger the observed anisotropy. Because hydrodynamics assumes practically infinite scattering rate and zero mean free path, it is often assumed to give an upper limit of anisotropy at fixed impact parameter (25). However, this upper limit depends on the EoS and, in principle, it is possible that hydrodynamical description with very soft EoS would give a smaller anisotropy than, for example, a microscopic cascade description (68).

If the freeze-out happens at the same temperature for all particle species, a signature of hydrodynamic flow is that the heavier the particle, the flatter the slope of its  $p_T$ -spectrum. Similarly, the  $p_T$ -averaged elliptic flow  $v_2$  increases when particle mass increases. However, the  $p_T$ -differential elliptic flow  $v_2(p_T)$  has the opposite behavior: The heavier the particle, the smaller the anisotropy at fixed  $p_T$ . The apparent discrepancy has a simple explanation:  $v_2$  is not an additive quantity, but when  $p_T$ -averaged  $v_2$  is calculated from  $p_T$ -differential  $v_2(p_T)$ , the latter is weighted by the particle distribution. Thus, the flatter  $p_T$  distribution of a heavier particle weights more the high- $p_T$  region, where  $v_2(p_T)$  is larger. Therefore, even if  $v_2(p_T)$  is smaller at all  $p_T$  for a heavier particle, the  $p_T$ -averaged  $v_2$  can be larger than  $v_2$  for a light particle. Whether this happens in practice and how large the differences are depend on the details of the flow profile, i.e. expansion dynamics, and the resonance decays.

The mass ordering of the low- $p_T$  anisotropy has its origin in the behavior of boosted particle distributions. As is well-known, transverse flow shifts the  $p_T$ -distributions to larger values of  $p_T$ . In the extreme case in which the speed of the collective motion is the same everywhere, as in the case of a thin shell expanding with a velocity  $v$ , the particle distribution develops a maximum at some finite  $p_T$  (the so-called blast wave peak (69)) and a local minimum at  $p_T = 0$ . The heavier the particle, the larger the  $p_T$  where the distribution peaks. Compared with a case without transverse flow, the particle yield is thus depleted at low  $p_T$ . The heavier the particle and the larger the flow velocity  $v_T$ , the larger the depletion. Correspondingly, if the flow velocity is larger in the in-plane than in the out-of-plane direction, the low- $p_T$  depletion is larger for particles moving in the in-plane direction than the out-of-plane direction and the overall anisotropy,  $v_2$ , is reduced. This reduction and the range in which it occurs increases with the particle mass and average transverse flow velocity. In the extreme case of

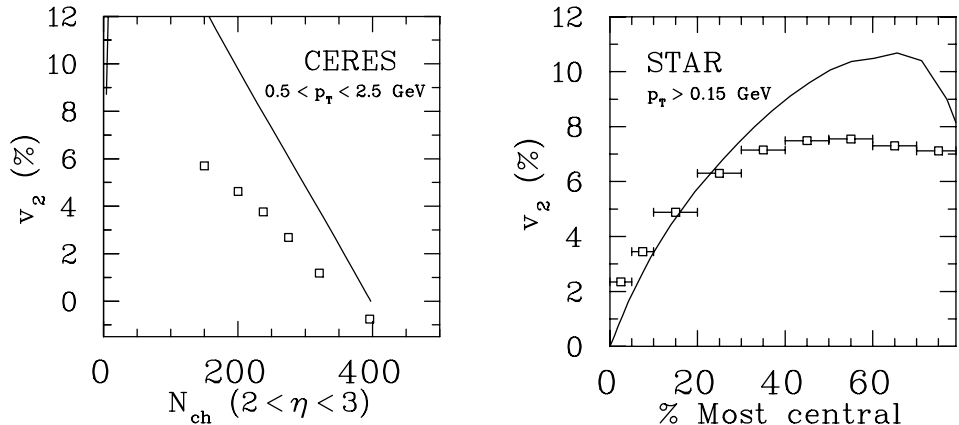


Figure 9: Elliptic flow  $v_2$  of charged hadrons as a function of centrality at (left panel) Pb+Au collisions at  $\sqrt{s_{NN}} = 17.3$  GeV measured by CERES (71) and at (right panel) Au+Au collisions at  $\sqrt{s_{NN}} = 200$  GeV measured by STAR (66). Hydrodynamical calculations are taken from References (31, 71). Note that the hydrodynamical results are not directly comparable because of different  $p_T$  cuts implemented.

a thin expanding shell, this reduction can be so strong that it reverses the sign of the anisotropy and  $v_2$  becomes negative. When the thin shell is replaced by a more realistic velocity profile, the peak in transverse-momentum distribution disappears. Similarly, a more realistic velocity distribution weakens the reduction of  $v_2$  at low  $p_T$ , but the mass ordering of  $v_2$  at low  $p_T$  remains. Whether some particles depict positive or negative  $v_2$  at low  $p_T$  depends on the details of the flow velocity of the source.

For relativistic  $p_T > m$ , the particle mass does not play any role in the thermal distribution and, consequently,  $v_2(p_T)$  of different particles converge. In a simple model in which the flow-velocity profile is replaced by its average value,  $v_2(p_T)$  increases with  $p_T$  and approaches unity asymptotically. The details of the flow-velocity profile can change this behavior, but so far no hydrodynamical calculation has reproduced the experimentally observed saturation of elliptic flow.

### 3.3.1 CENTRALITY DEPENDENCE

In a hydrodynamic description, the final anisotropy of particles is almost directly proportional to the geometrical anisotropy of the initial state (70). The proportionality is, however, nontrivial and depends on the applied decoupling criterion. When the impact parameter increases and the collision becomes more peripheral, the collision system becomes more and more elongated and its geometric anisotropy increases. We can thus expect the observed momentum anisotropy to increase as well. The data in Figure 9 shows increasing elliptic flow with decreasing centrality both at SPS and RHIC energies, but the magnitude of the flow differs from the hydrodynamical result. At SPS energy the data is consistently below the calculation, whereas at RHIC energy ( $\sqrt{s_{NN}} = 200$  GeV in Figure 9) the data is reproduced up to semi-central collisions but is below the calculation at peripheral collisions.

The failure of hydrodynamics to describe the anisotropy in most peripheral collisions and at SPS energy is often explained by a lack of necessary thermalization owing to the small size and/or particle number of the collision system (72). An alternative explanation assumes that the initial partonic state is sufficiently thermalized, but the final hadronic state has such a large viscosity that it cannot be modeled using ideal-fluid dynamics (73). The latter approach has been tested using so-called hybrid models in which the plasma phase and phase transition are described using ideal hydrodynamics, but the hadron phase is described using a cascade model (61, 73–75). The centrality dependence of  $p_T$ -averaged elliptic flow at RHIC has been reproduced nicely using such a hybrid approach (61, 73), but the results for  $p_T$  differential  $v_2$  at  $\sqrt{s_{NN}} = 200$  GeV collision energy are not available at the time of this writing.

At the beginning of this section it was argued that hydrodynamics leads to the largest possible anisotropy. However, at most central collisions at RHIC, the data tends to be above the hydrodynamical calculation. Fluctuations in the shape of the initial system may explain this. Owing to these fluctuations, the initial shape of some events in almost-central collisions can be in-plane elongated, even if the shape on most events is out-of-plane elongated. Thus elliptic flow is negative in some events, but because experimental analysis measures the magnitude of the anisotropy, not its sign, elliptic flow is measured as positive in all events and the measured value is larger than the average value. The initial state of hydrodynamical calculation, however, is an average initial state in which fluctuations of the spatial anisotropy cancel each other and the calculated anisotropy is smaller than measured (76). Preliminary calculations in which the initial-state fluctuations are included favor this interpretation by leading to better reproduction of the data (77).

The general trend is that a stiffer EoS and a lower freeze-out temperature lead to larger  $p_T$ -averaged flow if nothing else in the model is changed. This also changes the single particle distributions. If these are still required to fit the data, additional changes are required. For example, a stiffer EoS usually necessitates a higher freeze-out temperature. The combined effect largely cancels and the final  $p_T$ -averaged anisotropy is almost unchanged in semi-peripheral collisions in which a hydrodynamical description works best (31).

### 3.3.2 MOMENTUM and PARTICLE SPECIES DEPENDENCE

Hydrodynamic calculations at SPS and RHIC energies lead to anisotropy, which increases with increasing  $p_T$  and approaches unity asymptotically. Simple parametrizations of flow (so-called blast-wave models) also lead to this kind of behavior, which differs from experimental observations in which  $v_2$  saturates at high  $p_T$ . At mid rapidity, the agreement between the data and calculations depends on energy in the same way as for the centrality dependence: At SPS energies the calculations overestimate the data, whereas at RHIC energy a good agreement can be reached. The  $p_T$  range in which the data can be reproduced depends on the particle species. Charged hadrons and pions can be fit up to  $p_T \approx 1.5$  GeV, whereas protons follow the calculations up to  $p_T = 2.5$ –3 GeV in minimum-bias

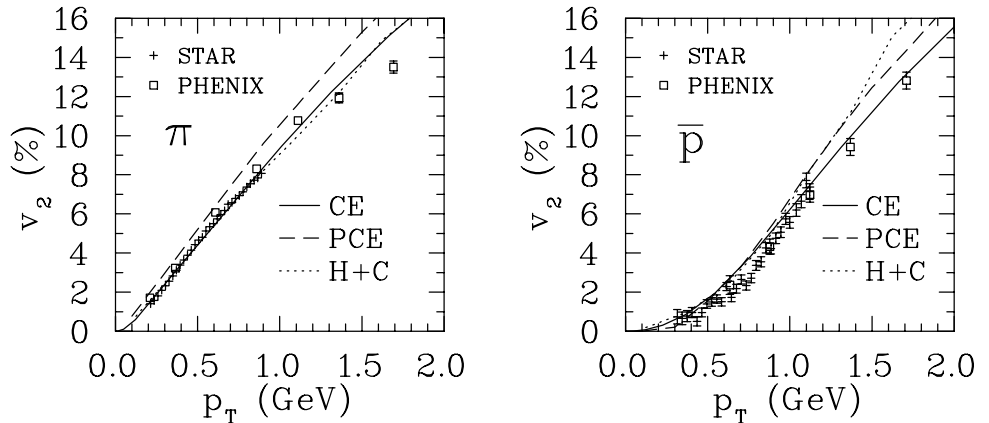


Figure 10: Pion (left panel) and antiproton (right panel)  $v_2(p_T)$  at midrapidity in minimum-bias Au+Au collisions at  $\sqrt{s_{NN}} = 200$  GeV. Hydrodynamical results are labeled CE for chemical-equilibrium result (31), PCE for chemical-nonequilibrium result ((40, 61); T. Hirano, personal communication) and H+C for hydro+cascade hybrid model at  $\sqrt{s_{NN}} = 130$  GeV energy (73). The data are taken by STAR (78) and PHENIX (79).

collisions. This behavior is qualitatively similar to that seen in Figures 4 and 5 for transverse momentum spectra, where hydrodynamically calculated spectra fit the data up to  $p_T \sim 3$  GeV.

A hydrodynamic description predicts a characteristic mass dependence of elliptic flow at low  $p_T$ . The higher the mass, the lower the  $v_2$ . How large this difference is depends on the details of the flow profile and therefore on the EoS. If chemical equilibrium in the hadronic phase is assumed, the differential anisotropy of pions can be well reproduced when the  $p_T$  spectra of pions is reproduced. In such a case, the proton  $v_2(p_T)$  depicts sensitivity to the phase transition. If the phase transition takes place in a narrow temperature interval and has large latent heat, the proton differential anisotropy can almost be reproduced. If there is no phase transition, the calculated proton anisotropy is clearly above the data (31). The status of strange particles is less satisfactory. Kaons and  $\Lambda$ -baryons show similar dependence on the EoS than protons, but the difference between the data and hydrodynamical calculation is larger than in the case of protons (31).

Unfortunately, it is not yet possible to use the apparent sensitivity of proton  $v_2(p_T)$  to the EoS to quantitatively constrain the EoS. If the requirement of chemical equilibrium is relaxed and one uses separate chemical and kinetic freeze-out temperatures, the fit to pion  $v_2(p_T)$  is lost (see Figure 10 and Reference (40)). However, if the hadronic phase is described using the RQMD transport model, as in Reference (73) for the  $\sqrt{s_{NN}} = 130$  GeV collision energy, the yields are correct and the  $v_2(p_T)$  is described as well as in the case of chemical equilibrium. Thus, there is a considerable uncertainty in the description of the hadronic stage of the evolution, which makes it impossible to draw final conclusions about the EoS needed to describe the differential anisotropy.

Another uncertainty here is the effect of viscosity. The ability of ideal-fluid hy-

drodynamics to reproduce the  $v_2$  data at RHIC has been interpreted to mean that the value of shear viscosity in QGP is particularly low (60, 80). However, viscosity has been estimated to decrease elliptic flow (4), and chemical non-equilibrium increases elliptic flow (40, 41). Hirano & Gyulassy have argued that the plasma has sufficiently low viscosity to allow its modeling using ideal hydrodynamics, but the dissipative effects in the hadronic phase are the reason for the failure of chemically non-equilibrium hydrodynamics to describe the data (60). This claim seems to be validated by the ability of hybrid models to describe the data, but final conclusions must wait for the complete results of hybrid calculations and the results of viscous calculations (5, 81).

### 3.3.3 PSEUDORAPIDITY DEPENDENCE

The  $p_T$ -averaged elliptic flow has quite a strong dependence on pseudorapidity (78, 82–84). In a narrow region around midrapidity,  $|\eta| < 1$ , elliptic flow remains approximately constant (78, 85) but decreases strongly towards larger pseudorapidities. However, charged particle multiplicity depicts much wider plateau around midrapidity than elliptic flow (86).

The purely hydrodynamical calculations have not reproduced the pseudorapidity dependence of elliptic flow, although the same calculations reproduce the multiplicity as a function of pseudorapidity (40, 87). However, a hybrid model that reproduces the centrality dependence of elliptic flow also gives a reasonable description of its pseudorapidity dependence (61). The failure of ideal-fluid hydrodynamics has been interpreted in the same way as in the case of centrality dependence – either as an incomplete thermalization of the system at large rapidities from the beginning (72) or as an effect of viscosity and incomplete thermalization at the late stage (61). There are also other open questions in the hydrodynamic treatment that may affect the results: The initial shape of the system, large deviations from boost-invariant flow, and different thermalization time and freeze-out temperature at different rapidities could all affect the final anisotropy and are mostly unexplored. It is therefore possible that the thermalized region where hydrodynamics works at RHIC energy is relatively narrow in rapidity, but final conclusions cannot be drawn yet.

## 3.4 Two-Particle Bose-Einstein Correlations

Information about the space-time structure of the system formed in a heavy-ion collision can be obtained by measuring the low-momentum correlations of identical particles. For bosons these correlations are called Bose-Einstein correlations and the method for their interpretation is called HBT interferometry according to the originators of this method (88). Here we show only the basics of the HBT formalism as applied to hydrodynamical models and its most important results. A detailed explanation about this technique can be found in Reference (89), and the present status is discussed in recent reviews (90, 91). HBT in hydrodynamical context is more thoroughly discussed in Reference (92).

Intensity interferometry is based on an analysis of the two-particle momentum

correlation function,

$$C(\mathbf{q}, \mathbf{K}) = \frac{E_1 E_2 \frac{dN}{d^3\mathbf{p}_1 d^3\mathbf{p}_2}}{E_1 \frac{dN}{d^3\mathbf{p}_1} E_2 \frac{dN}{d^3\mathbf{p}_2}}, \quad (11)$$

that is, the ratio of a two-particle distribution and a product of two one-particle distributions. The correlator is usually written in terms of the momentum difference between the two particles,  $q = p_1 - p_2$ , and their average momentum,  $K = \frac{1}{2}(p_1 + p_2)$ . If the particles are emitted independently (“chaotic source”) and propagate freely from the source to the detector, the two-particle distribution is not equal to the product of one-particle distributions. At small values of relative momentum  $q$ , it is larger than the product of one-particle distributions owing to quantum statistical (wave-function symmetrization) effects.

If there are no final-state interactions (or the spectra are corrected for them), the two-particle correlator  $C(\mathbf{q}, \mathbf{K})$  is related to the emission function  $S(x, K)$ :

$$C(\mathbf{q}, \mathbf{K}) \approx 1 + \left| \frac{\int d^4x S(x, K) e^{iq \cdot x}}{\int d^4x S(x, K)} \right|^2. \quad (12)$$

The emission function  $S(x, K)$  is the Wigner phase-space density of the emitting source. In the derivation of Equation 12 the emission function is assumed to be sufficiently smooth, i.e.  $S(x, K) \approx S(x, K + \frac{1}{2}q)$  (see Reference (89)). Because both  $p_1$  and  $p_2$  are on-shell, the average momentum  $K$  is, strictly speaking, off-shell. In practice, however, on-shell approximation for  $K$  is used:  $K_0 \approx \sqrt{\mathbf{K}^2 + m^2}$ .

In the hydrodynamic approach the quantum-mechanical Wigner phase-space density is replaced by a classical phase-space density at the time of freeze-out. When Cooper-Frye formalism is applied, it is given by

$$S(x, K) = \frac{g}{(2\pi)^3} \int \frac{d\sigma_\mu(x') K^\mu \delta^4(x - x')}{\exp\{[K \cdot u(x') - \mu(x')]/T(x')\} \pm 1}. \quad (13)$$

It is not possible to define uniquely the source function  $S(x, K)$  from the measured correlation function  $C(\mathbf{q}, \mathbf{K})$ . The experimental data of two-particle correlations are therefore presented using some ansatz for the the source function. Usually this is done using a Gaussian form for the correlator. If the collision system is further approximated to be boost-invariant, the correlator for central collisions can be written in a particularly simple form in terms of three HBT radii:

$$C(\mathbf{q}, \mathbf{K}) \approx 1 + \exp[-R_o^2(K_T)q_o^2 - R_s^2(K_T)q_s^2 - R_l^2(K_T)q_l^2]. \quad (14)$$

In this so-called Bertsch-Pratt parametrization, the coordinate directions are defined in such a way that out- ( $R_o$ ) and long-direction ( $R_l$ ) are parallel to  $\mathbf{K}_T$  and beam, respectively, whereas the side-direction ( $R_s$ ) is perpendicular to both  $\mathbf{K}_T$  and beam. In a boost-invariant approximation, the radii depend only on the magnitude  $K_T$  because the particle emission in central collisions does not depend on the azimuthal angle  $\phi$  and boost-invariance means that there cannot be any rapidity dependence.

These radii do not correspond to the actual physical size of the source, but rather characterize so-called regions of homogeneity, the regions where particles

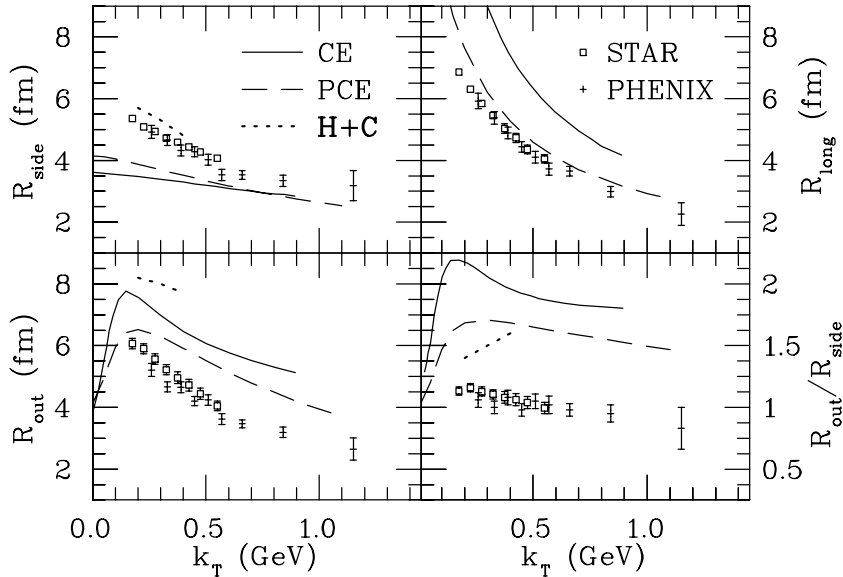


Figure 11: Pion source radii in Au+Au collisions at  $\sqrt{s_{NN}} = 200$  GeV. Hydrodynamical results are labeled CE for boost-invariant chemical-equilibrium result (26), PCE for nonboost-invariant result with separate chemical and kinetic freeze-outs ((40, 61); T. Hirano, personal communication) and H+C for hydro+cascade hybrid model (94). The data are taken by the STAR (95) and PHENIX (96) collaborations.

with particular  $p_T$  are most likely emitted. For a Gaussian source, the HBT radii measure the following different combinations of space-time variances of the system (92):

$$R_s^2(K_T) = \langle \tilde{x}_s^2 \rangle(K_T) \quad (15)$$

$$R_o^2(K_T) = \langle (\tilde{x}_o - \beta_\perp \tilde{t})^2 \rangle(K_T) \quad (16)$$

$$R_l^2(K_T) = \langle \tilde{x}_l^2 \rangle(K_T), \quad (17)$$

where  $\beta_\perp = K_T/K^0$  is the transverse pair velocity, and space-time coordinates  $\tilde{x}$  are defined as distances from the “effective source center”  $\tilde{x}^\mu(K_T) = x^\mu - \langle x^\mu \rangle(K_T)$ , where brackets denote weighted averages over the source function  $S(x, K)$ :

$$\langle f(x) \rangle(K) = \frac{\int d^4x f(x) S(x, K)}{\int d^4x S(x, K)}. \quad (18)$$

The radii are thus independent of the actual coordinates of the emission, but are sensitive to variances of the geometry.

Hydrodynamic calculations for RHIC energies predicted that a phase transition from a plasma to a hadron gas would increase the lifetime of the system (93). The long lifetime would increase the  $\beta_\perp \tilde{t}$  term in Equation 16 and thus increase the  $R_o$ -radius and make the ratio  $R_o/R_s$  large. The experimental data, however, shows no sign of this kind of effect and yields a ratio of  $R_o/R_s \approx 1$ .

Figure 11 shows some of the hydrodynamic calculations for the HBT radii at RHIC energy. Hydrodynamic calculations with assumed boost-invariance, chemical equilibrium, and a first-order phase transition (CE, solid line) tend to lead

to a too small sideward radius  $R_s$ , too large outward and longitudinal radii  $R_o$  and  $R_l$ , respectively, and especially to a too large ratio  $R_o/R_s$  (26). Both  $R_o$  and  $R_l$  can be made smaller if the system decouples sooner, i.e. in higher temperature, but such an approach leaves  $R_s$  basically unchanged and distorts the single particle spectra (26, 92). To a lesser extent, the same effect can be achieved by decreasing the initial time or increasing the transverse flow by a non-zero initial velocity field, but neither of these approaches changes the too small  $R_s$  (26).

Another way to reduce the longitudinal radius  $R_l$  is to relax the boost-invariant approximation (40, 97). When this approach is used with an EoS with separate chemical and kinetic freeze-outs (PCE, dashed line),  $R_l$  is close to the data. Both  $R_o$  and  $R_s$  move closer to the data but are still too large and small, respectively. This approach also leads to problems with the elliptic anisotropy (see chapter 3.3).

An approach that brings  $R_s$  close to the data chooses a wide but flat initial distribution (97), which leads to slower buildup of flow from an initially larger source. In that case, the problem is again  $R_o$ , which is too large. This is expected because  $R_o$  is sensitive to the lifetime of the system, which becomes relatively large in this approach.

One way to reduce the lifetime of the system and thus  $R_o$  is to change the EoS. As mentioned, one of the suggested signatures of a first-order phase transition is a long lifetime and large  $R_o$ . If one uses an EoS with a smooth crossover instead of a first-order phase transition,  $R_o$  decreases and  $R_s$  increases (98). Unfortunately, even in that case, no good fit to the data is achieved. It is also questionable how this change in EoS would affect the elliptic anisotropy (31).

Grassi et al. have suggested that the discrepancy between the data and calculations is due to too simple a treatment of freeze-out on a sharp hypersurface, and a more realistic continuous emission of particles would lead to better results (99). However, when this is accounted for effectively in hybrid models in which the hadronic stage is described using a cascade transport model, the results are even worse (94). The particles are emitted from larger, longer-lasting volume than in a simple hydrodynamic description, and correspondingly,  $R_s$  is larger and reproduces the data (H+C, dotted line in Figure 11). Unfortunately, the longer lifetime also leads to an even larger  $R_o$ .

Another possible reason for the discrepancy between the data and calculations is viscosity (4, 100). Initial calculations (5) show that it has the desired effects, but whether they are large enough remains to be seen. Again, the effect of viscosity on elliptic flow is large, and it is unknown if a viscous model could reproduce both the HBT radii and elliptic anisotropy.

## 4 ELECTROMAGNETIC EMISSION

All the observables described in the previous section 3 are hadronic observables. By definition, the hadrons of the system interact with each other, and the distributions and yields of hadrons are fixed late in the evolution of the system, when interactions cease, the distributions and yields freeze out, and the particles decouple. Therefore, those observables characterize the properties of the particle-

emitting source at the end of the system evolution, but not the history of the system during the evolution. In principle, it is possible to have very different dynamics producing similar final states.

Possible observables that are sensitive to the entire evolution of the collision system are photon and lepton-pair distributions. Because these particles interact only electromagnetically, their mean free paths are much longer than those of hadrons. They can thus escape the collision system without rescattering and carry information about the conditions in which they were formed. However, the photon and dilepton spectra get contributions from all stages of the evolution, which makes it difficult to disentangle the signal coming from the hot, dense stage of the collision. To describe the different contributions to electromagnetic spectra, we follow the terminology of Reference (101):

- prompt photons and leptons are produced in the primary collisions of incoming partons;
- thermal photons and leptons are emitted in the collisions of quarks and gluons during the plasma phase and in the collisions of hadrons in the hadronic phase;
- decay photons and leptons are decay products of hadrons;
- direct photons and leptons are the sum of prompt and thermal photons.

The thermal photon production depends strongly on temperature via the factor  $\exp(-p_T/T)$ . Therefore the early stage, when the matter is hottest, should dominate the photon emission, and the measurement of photon spectra should be an effective thermometer for the temperature achieved in the collision. However, prompt photons follow a power-law distribution  $p_T^{-n}$  and dominate at high  $p_T$ .

The hydrodynamic model can be used to calculate the thermal and decay contributions, but the prompt photons and leptons require a separate pQCD calculation. The calculation of decay photons is relatively straightforward, and it proceeds in the same way as the calculation of hadron spectra from resonance decays described in section 3.1. One calculates the distribution of hadrons at freeze-out and applies the relevant decay kinematics and branching ratios to get the spectra of decay photons and leptons. To calculate the thermal yield, the production rate of photons or leptons in a thermal system,  $dR/d^3p(E, T, \mu)$ , has to be integrated over the space-time volume of the system:

$$E \frac{dN}{d^3p} = \int d^4x \left\{ \begin{aligned} & w(\varepsilon, \rho_B) E \frac{dR^{\text{QGP}}}{d^3p}(p \cdot u, T, \mu_B) \\ & + [1 - w(\varepsilon, \rho_B)] E \frac{dR^{\text{HG}}}{d^3p}(p \cdot u, T, \mu_B) \end{aligned} \right\}, \quad (19)$$

where the production in a plasma and in a hadron gas (HG) is written separately. The factor  $w(\varepsilon, \rho_B)$ , which expresses the volume fraction of plasma, is unity in the plasma phase, zero in HG and between unity and zero in a mixed phase. Hydrodynamics provides the space-time evolution of the system, whereas the production rates in thermal matter are an input independent of hydrodynamics.

In the plasma phase, the photon production is dominated by the QCD Compton and annihilation reactions,  $qg \rightarrow q\gamma$ ,  $\bar{q}g \rightarrow \bar{q}\gamma$ , and  $q\bar{q} \rightarrow g\gamma$ . In lowest order, the production rate due to these processes was calculated in References (102, 103). However, some formally higher-order processes are strongly enhanced by collinear singularities and also contribute to order  $\alpha_s$  (104, 105). The resummation of these contributions was shown to be possible and was carried out by Arnold et al. (106), completing the order  $\alpha_s$  analysis of the photon-emission rate. A parametrization of the rate was also given in Reference (107).

The calculation of the photon-production rate in a hot hadron gas is less complete than the rate in a plasma owing to the multitude of different hadron species and photon-producing interactions and owing to the model dependence of the calculations (see References (101, 108)). The standard rate in the literature is the one calculated in Reference (102), where photon production in scattering and decay processes  $\pi\pi \rightarrow \rho\gamma$ ,  $\pi\rho \rightarrow \pi\gamma$ ,  $\omega \rightarrow \pi\gamma$ , and  $\rho \rightarrow \pi\pi\gamma$  was calculated using pseudoscalar-vector Lagrangian with coupling constants determined from free  $\rho$  and  $\omega$  decays. These rates are often supplemented with a production rate via  $a_1$ -mesons from Reference (109).

The role of different channels in photon production was further studied using chiral Lagrangians (110). Unfortunately, it was not possible to fix the model parameters unambiguously in this work, which led to a factor of three uncertainty in the final rates. In the context of dilepton production, it was later possible to fix the model parameters much better (111), and this approach was used in a recent calculation by Turbide et al. (112). In that work, the study was extended to cover photon emission from heavier meson resonances, strange particles, and baryons. Another recent analysis of photon production from a hadron gas was done by Haglin (113), who studied the effect of strange particles and higher-order processes achieving a rate larger than the standard rate (102) by a factor of two at large  $q_T$  and by an order of magnitude at low  $q_T$ .

There are still uncertainties in the calculation of the photon-production rate in hot hadron gas. Surprisingly, even after all the improvements in the calculations, the statement made in Reference (102) is still valid. At the same temperature, the production rate per unit volume in a plasma and a hot hadron gas is approximately equal, and they both “shine as brightly”. However, the emission rate per unit entropy is larger in hadron gas.

The main contribution to dilepton production in plasma comes from the annihilation process  $q\bar{q} \rightarrow l\bar{l}$ . The rate calculated in lowest order in a baryon-free plasma can be found in textbooks (114) and was calculated for finite baryon chemical potentials in Reference (115). At small values of invariant lepton-pair mass, corrections of the order  $\alpha\alpha_s$  to this rate become important (116), but in heavy ion collisions lepton pairs from Dalitz decays of final mesons produce a larger background (117). Multi-loop calculations similar to those done to calculate the photon rate have also been carried out for high- $p_T$  pairs with small invariant mass (118). These calculations have resulted in rates somewhat larger than the first-order calculations. First attempts to calculate lepton production using a lattice-QCD formalism have also been done (119). The preliminary re-

sults are quite close to the perturbative rate, at least in some parts of the phase space.

The observation of large excess dileptons in the mass region below the  $\rho$ -meson mass in Pb+Au collisions at  $\sqrt{s_{NN}} = 17.3$  GeV energy at the CERN-SPS (120) has fueled considerable theoretical interest in studying the lepton-pair emission in a hot hadronic gas (108, 121). The main problem of these studies has been whether and how the properties of mesons change in medium and how these changes are reflected in the rates. A rate calculated by Gale & Lichard (122) using free-particle properties is often used as a benchmark in comparisons with more sophisticated approaches. In the calculations of Rapp et al. (123) and Eletsky et al. (124), the basic assumption is that the spectral density of  $\rho$ -meson changes in medium. These calculations are technically very different, but produce qualitatively similar rates (125). An alternative approach pursued by Brown & Rho (126) assumes that the  $\rho$ -meson mass decreases in the medium.

#### 4.1 Photons at SPS

Direct photon production in  $\sqrt{s_{NN}} = 17.3$  GeV Pb+Pb collisions at the CERN-SPS was measured by the WA98 collaboration (127). Several authors have compared this data with hydrodynamical calculations (128–132). All authors agreed that the photon spectrum could be explained if one assumes sufficiently hot ( $T > 200$  MeV) initial state, but the required initial temperature varied largely from  $T \sim 200$  MeV (129) to  $T = 335$  MeV (128). The large difference is owing mainly to different assumptions in the calculations.

One factor that explains the largely varying initial temperature is the use of different rates in a hadron gas. Alam et al. (129) assumed in-medium modifications to hadron properties both in the EoS and in production rates, which enhance the photon emission at lower temperatures, allowing cooler initial state. The full order  $\alpha_S$  rate for photon production in plasma was used only in the most recent paper (132), but at SPS energy the different rates in plasma cause significant differences in the final yield only at relatively large values of  $p_T$ .

The initial state of the system was also chosen in different ways in different calculations. Especially, the assumption of finite transverse flow velocity at the beginning of the hydrodynamic evolution leads to lower temperatures. Because the rates are proportional to  $\exp(-p \cdot u/T)$ , where  $p$  is the four momentum of the photon and  $u$  is the flow four-velocity, stronger transverse flow allows lower temperatures to produce equal yield at high  $p_T$ . Peressounko & Pokrovsky (130) argued the necessity of such an initial flow, and Alam et al. (129) and Chaudhuri (131) later studied its effects. It can be argued that gradients in initial particle production would lead to buildup of flow during thermalization, but it is very difficult to quantify how large flow velocities could build up this way. Peressounko & Pokrovsky also argued that the pion spectra especially necessitates the initial flow, but the authors of this review have not been able to fit the hadron spectra if initial transverse flow is assumed.

The hadron spectra were reproduced in References (130, 132), and, when no initial transverse flow is assumed, also in Reference (129). In the other two cal-

culations (128, 131), the initial state was only required to have the same entropy as the final-state particles. It is thus unknown whether these calculations are consistent with the hadron data.

With the exception of Reference (132), boost-invariant hydrodynamics was used in these calculations. If high initial temperature is required, this assumption leads to short initial, i.e. thermalization, time,  $\tau \sim 0.2 \text{ fm}/c$  (128). At SPS energy it can be argued that such a short initial time is ambiguous because the longitudinal extension of the colliding nuclei is larger than  $c\tau_0$ . This makes the application of boost-invariant expansion uncertain for times  $\tau < 1 \text{ fm}/c$ . In Reference (132) this problem was solved by using nonboost-invariant hydrodynamics, where longitudinal geometry is explicit and the initial time does not appear. Also, the ambiguity in choosing the initial state was studied and it was shown that several EoSs and initial states reproduced both the hadron and photon data (132, 133).

To characterize the results, Figure 12 shows the photon spectrum calculated in Reference (132) and compares it with WA98 data. The calculation was done using two different equations of state (EoS A and H) and two different initial states (IS 1 and IS 2). EoS A contains a phase transition from hadron gas to quark-gluon plasma at  $T_c = 165 \text{ MeV}$  whereas EoS H is a purely hadronic equation of state. IS 1 has a very peaked initial density distribution in the longitudinal direction, whereas IS 2 has a flatter distribution (see Reference (133)) and smaller maximum temperature, which is more consistent with the assumption of hadronic EoS. In both cases, the hadron spectra are reproduced and, as shown in the figure, the calculated photon spectrum is within the experimental error bars. Thus, the conclusion of the hydrodynamic studies of photon emission at the SPS is that high temperature initial state is needed to reproduce the measured photon spectra, but a phase transition to plasma is not necessarily required.

#### 4.2 Photons at RHIC

At the time of this writing, the situation of the photon data at RHIC is becoming very interesting: Preliminary data presented (135) at the latest Quark Matter 2005 meeting indicates a clear excess of photons over decay and prompt photons in the transverse-momentum range up to  $\sim 3 \text{ GeV}$ . Earlier measurements have been inconclusive owing to the large error bars, but the new method to extract the photon yield from the measurements of low-mass  $e^+e^-$  pairs appears more promising, and if the preliminary results are confirmed by the full analysis, this data offers a long-sought direct probe into the earliest moments of the collision.

Many authors have predicted the photon emission at RHIC and the LHC (101, 105, 129, 136–141). Owing to uncertainties in the initial state, these predictions serve mostly as order-of-magnitude estimates, but they also address the question of whether the thermal photon yield would be larger than the prompt photon yield at any value of  $p_T$ . The initial conditions of more recent studies have been constrained to produce the total hadron multiplicity, and in Reference (101), the thermal photons are compared with the calculated yields of decay photons both from thermal pions and prompt pions from jet fragmentation. The measured

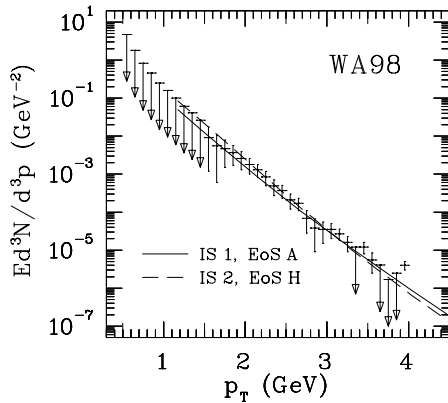


Figure 12: The sum of thermal photon emission at the SPS from hydrodynamic calculation (132) and prompt photon emission (134) compared with WA98 data (127).

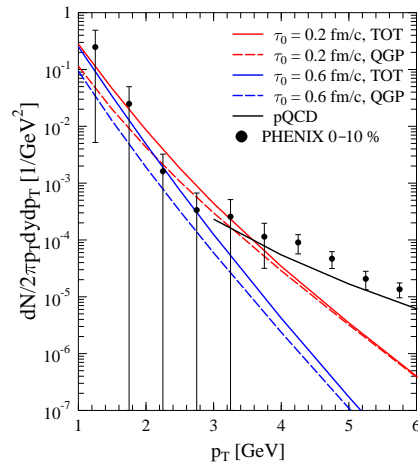


Figure 13: Thermal photon emission at RHIC from hydrodynamic calculation using two different initial times. Solid lines labeled TOT indicate the total yield of thermal photons whereas dashed lines indicate emission from plasma. The pQCD calculation for prompt photons (101) and preliminary PHENIX data (135) are also shown.

spectrum of  $\pi^0$ 's is compared with the calculations and the data is well described. The hydrodynamical calculations with the same initial conditions are also compared with other hadron data and the overall agreement is very good (44). The perturbative QCD calculation to NLO in all quantities entering the calculation is supplemented with the energy loss of produced jets in the thermal matter.

The main conclusions from the studies in (101), supported for the hadron observables by (44), are as follows: The understanding of the hadron spectra in terms of hydrodynamic and pQCD calculations is quite good. This means that the photons from hadron decays are well under control when comparing different sources in the calculations. The other main sources of photons are prompt photons from primary interactions, including the photons from jet fragmentation, and the photons from secondary interaction in produced matter, the thermal photons<sup>3</sup>. These photon sources have quite distinct transverse-momentum dependence with the cross-over from thermal photons to prompt photons taking place at around  $p_T \sim 3$  GeV, the region where the behavior of the preliminary data also changes.

The simplest hydrodynamic calculations assume a scaling expansion in the longitudinal direction and ignore the transverse expansion. The qfirst assumption can be argued to be reasonable in the central rapidity region because at RHIC

<sup>3</sup>More generally the photons from secondary interactions among the produced particles can originate also from non-thermal processes like a high-energy quark producing photons when Compton scattering from a lower energy thermal gluon (142).

energy the Lorentz gamma factor is  $\sim 100$ , indicating a time interval on the order of  $0.1 \text{ fm}/c$  for the nuclei to pass through one another. This is shorter than the shortest initial times used in the calculations. In the central rapidity region, the longitudinal components are not large and the acceleration of the longitudinal expansion is small, having little effect on the multiplicity density or the freeze-out time at  $y \approx 0$  (143). Ignoring the transverse expansion cannot be justified, except for the photons emitted at the earliest times from the QGP. High- $p_T$  photons from QGP are almost insensitive to flow because they are emitted when the system is hottest (141), but the strong flow at the late hadronic stages enhances the emission of high- $p_T$  photons from hadron gas (129).

Predictions of the relative size of photon contributions at different values of  $p_T$  vary somewhat. For example, Srivastava (140) predicts that at RHIC energy, the photons from the QGP dominate at small values of  $p_T$ , i.e.,  $p_T < 1 \text{ GeV}$ , and the thermal photons at high  $p_T$  come mainly from the hadronic phase. More recent calculations lead to a conclusion that at RHIC multiplicity the contribution from plasma dominates for  $p_T > 3$ , and at smaller transverse momenta the contribution from plasma and hadron gas are the same size, with the latter slightly larger at smallest momenta (136, 138). The rates used in the calculations is one reason for the difference: In Reference (140) older rates that do not include all order of  $\alpha_S$  terms are utilized, whereas the newer calculations are based on the full order of  $\alpha_S$  (107) results. Also, note that the dependence of the plasma contribution depends strongly on the assumed thermalization time,  $\tau_0$ . When comparing different predictions the first detail to be checked is  $\tau_0$ , see Reference (101).

Although the pQCD calculation of prompt photons is not entirely under control at small transverse momenta owing to the uncertainty in the photon fragmentation functions (see discussion in References (101, 144)), the photon yield from secondary collisions, i.e. the yield of thermal photons, decreases more steeply and becomes negligible for  $p_T \gtrsim 4 \text{ GeV}$ . In the calculations thermal and prompt photons become comparable at around  $p_T \sim 3 \text{ GeV}$ , and because of the difference in the slopes, the uncertainty in where the contributions cross is not large. At small momenta below  $3 \text{ GeV}$ , thermal photons dominate (136, 138), but it is not clear whether this contribution is so large that it can be isolated from the pion decay background.

Different contributions are compared with the preliminary photon data (135) in Figure 13. Here, initial times  $\tau_0 = 0.2$  and  $0.6 \text{ fm}/c$  are used in the hydrodynamical calculation, which correspond to average initial temperatures  $\langle T \rangle = 340$  and  $250 \text{ MeV}$ , respectively. In the prompt photon calculation no intrinsic  $k_T$  is included because the same calculation for photon production in  $p + p$  collisions at RHIC describes the data well. As indicated in Figure 13, the uncertainty in initial time causes more than an order of magnitude change in the thermal photon yield at high  $p_T$ .

In most calculations for thermal photons at RHIC and the LHC, chemically equilibrated matter is assumed. However, it can be expected that the initial state is gluon dominated and quarks are suppressed compared to their equilibrium yields (145). This would lead to smaller emission rates at a given temperature,

but the suppression of quarks means effectively smaller number of degrees of freedom and a larger temperature for a given entropy. Detailed calculations (101, 146) have indicated that these two effects largely cancel each other and that the final thermal spectra are quite similar in both equilibrium and non-equilibrium scenarios.

### 4.3 Dilepton calculations

Like the photon measurements, the dilepton mass spectrum at the SPS collisions measured by the CERES (120, 147) and NA50 (148) collaborations has been compared to hydrodynamical calculations several times (35, 125, 129, 133, 149–152). The low-mass dilepton ( $M_{ll} < m_\phi$ ) yield measured by CERES is dominated by emission from the late hadronic phase (see, e.g. Reference (151)) and constrains only the properties of the hadronic stage of the evolution. All these calculations agree that if meson properties in vacuum are used (122), the thermal yield is not quite sufficient to explain the observed excess. Thus, the experimental data seems to require modifications in meson properties, but so far the mass resolution has not been good enough to differentiate between a change in mass and changes in spectral density. Recently, there has been new preliminary data with better mass resolution (153, 154), but the conclusions are still being debated (155).

Kvasnikova et al. (152) addressed the intermediate-mass ( $m_\phi < M_{ll} < m_{J/\Psi}$ ) dilepton yield measured by NA50. In their calculation they found that the excess in lepton pairs in this mass region could be explained by thermal emission in the same way as in the low-mass region. Even if the intermediate-mass region is expected to provide a window for observing the emission from plasma (156), they found that a modest contribution from plasma,  $\sim 20\%$ , was enough to fit the SPS data.

So far the genuinely hydrodynamic calculations of dilepton emission at RHIC have been rare, and different parametrizations for the space-time evolution of the system have been used instead (123). Medium modifications to meson properties depend on total baryon density,  $\rho_{tot} = \rho_B + \rho_{\bar{B}}$ . Because  $\rho_{tot}$  at RHIC is essentially the same as at the SPS, the low mass dilepton spectrum at RHIC should show similar excess as seen at the SPS (123).

At intermediate masses, the thermal yield is expected to be dominated by emission from plasma (157). However, owing to a larger  $c\bar{c}$  production than at the SPS, the intermediate-mass dilepton yield can be dominated by correlated charm decays, unless the  $c$ -quarks rescatter significantly in the medium or can be identified and subtracted. Isotropization of  $c$ -quark momentum distributions would soften the dilepton mass spectrum, leaving a mass range in which thermal emission dominates (157, 158). An additional source of lepton pairs at RHIC is the interaction of jets with the surrounding dense plasma. According to recent calculations (159), the jet-plasma interactions may dominate over thermal dilepton emission at intermediate masses.

At the time of this writing there are no calculations in which all these contributions are taken into account and are folded with a realistic time-evolution of the collision system. It will be interesting to see how the future data will look

and if a contribution from plasma is needed to explain the data. The PHENIX collaboration has recently shown the first preliminary data of low-mass dileptons at RHIC (160), but the present experimental uncertainties are too large to draw any conclusions. These experimental shortcomings are currently being addressed by a detector upgrade (161).

## 5 CONCLUDING REMARKS

Hydrodynamics provides a well-defined framework to study many experimentally accessible features of a heavy ion collision. Some parts of the collision, such as the primary particle production of final-state matter, lie outside hydrodynamics, and some features of hydrodynamics, such as the freeze-out of final hadrons, have grave uncertainties. Nevertheless, a hydrodynamic description has robust features such as the conservation laws, which are strictly enforced. The main assumption of hydrodynamics, the occurrence of frequent collisions in the final state, can also convincingly be argued for from the large observed multiplicity. Hydrodynamics describes the effects of collisions among the constituents, in particular the momentum transfer between adjacent regions, in terms of pressure that arises microscopically from momentum transfer in the collisions. This should be a good approximation as soon as the momentum distribution of constituents is approximately isotropic.

Hydrodynamics describes well the broadening and its mass dependence of hadron spectra resulting from the increase of transverse collective motion (flow). The collective motion can also be seen in the elliptic flow. At low transverse momenta, the observed elliptic flow can be described using hydrodynamics. Especially, the observed mass ordering is typical for a hydrodynamic description. These are partly genuine predictions of hydrodynamics because the amount of initial production is fixed from the total multiplicity. Once the hadronic observables are under control, the largest remaining uncertainty concerns the time scales of primary production and of (approximate) thermalization. Electromagnetic emission is very sensitive on these time scales, and the preliminary results on photon emission at RHIC may be the first indication that emission from the early moments of the collision can be resolved. The emission of lepton pairs around and below the  $\phi$ -meson mass, offers both a stringent test of the hydrodynamic description of the hadron phase and a tool to study the effects of medium on the properties of vector mesons. The amount of information that can finally be obtained, depends a good deal on the progress in experimental measurements, but it is likely that hydrodynamics will remain an important tool for phenomenological studies for a long time.

## Acknowledgments

We would like to thank K. Eskola, H. Niemi, S.S. Räsänen and T. Hirano for discussions, H.N. and S.S.R. for help in preparing the figures and T.H. for allowing us to show some of his unpublished results.

## LITERATURE CITED

1. McLerran LD, *Acta Phys. Polon.* B30:3707 (1999)
2. Bjorken JD. *Phys. Rev. D* 27:140 (1983)
3. Rischke DH. arXiv:nucl-th/9809044
4. Teaney D. *Phys. Rev. C* 68:034913 (2003)
5. Muronga A, Rischke DH. arXiv:nucl-th/0407114
6. Muroya S, Sasaki N. *Prog. Theor. Phys.* 113:457 (2005)
7. Eskola KJ. *Nucl. Phys.* A702:249 (2002)
8. McLerran L, Venugopalan R. *Phys. Rev. D* 49:2233 (1994); *ibid.* 3352; *Phys. Rev. D* 50:2225 (1994)
9. Gribov LV, Levin EM, Ryskin MG. *Phys. Rep.* 100:1 (1983)
10. Ranft J. *Phys. Rev. D* 51:64 (1995)
11. Eskola KJ, Kajantie K, Ruuskanen PV, Tuominen K. *Nucl. Phys.* B570:379 (2000)
12. Eskola KJ, Kajantie K, Lindfors J. *Nucl. Phys.* B323:37 (1989)
13. Eskola KJ, Ruuskanen PV, Räsänen SS, Tuominen K. *Nucl. Phys.* A696:715 (2001)
14. Kovchegov YV. *Phys. Rev. D* 54:5463 (1996)
15. Jalilian-Marian J, Kovner A, McLerran LD, Weigert H. *Phys. Rev. D* 55:5414 (1997)
16. Kovchegov YV, Tuchin K. *Phys. Rev. D* 65:074026 (2002)
17. Krasnitz A, Venugopalan R. *Nucl. Phys.* B557:237 (1999)
18. Krasnitz A, Venugopalan R. *Phys. Rev. Lett.* 84:4309 (2000)
19. Krasnitz A, Venugopalan R. *Phys. Rev. Lett.* 86:1717 (2001)
20. Krasnitz A, Nara Y, Venugopalan R. *Phys. Rev. Lett.* 87:192302 (2001)
21. Krasnitz A, Nara Y, Venugopalan R, *Nucl. Phys.* A717:268 (2003)
22. Lappi T. *Phys. Rev. C* 67:05490 (2003)
23. Kharzeev D, Levin E, *Phys. Lett.* B523:79 (2001)
24. Kolb PF et al. *Nucl. Phys.* A696:197 (2001)
25. Heinz UW, Kolb PF. *Nucl. Phys.* A702:269 (2002)
26. Heinz UW, Kolb PF. arXiv:hep-ph/0204061
27. Baier R, Mueller AH, Schiff D, Son DT. *Phys. Lett.* B502:51 (2001)
28. Mrowczynski S. *Acta Phys. Polon.* B 37:427 (2006)
29. Rajagopal K. *Acta Phys. Polon.* B 31:3021 (2000)
30. Braun-Munzinger P, Magestro D, Redlich K, Stachel J. *Phys. Lett.* B518:41 (2001)

31. Huovinen P, *Nucl. Phys.* A761:296 (2005)
32. Venugopalan R, Prakash M. *Nucl. Phys.* A546:718 (1992)
33. Kapusta JI, Olive KA. *Nucl. Phys.* A408:478 (1983)
34. Rischke DH, Gorenstein MI, Stoecker H, Greiner W. *Z. Phys. C* 51:485 (1991)
35. Sollfrank J et al. *Phys. Rev. C* 55:392 (1997)
36. Broniowski W, Florkowski W. *Phys. Rev. Lett.* 87:272302 (2001)
37. Eskola KJ, Niemi H, Ruuskanen PV, Räsänen SS. *Phys. Lett.* B566:187 (2003)
38. Bebie H, Gerber P, Goity JL, Leutwyler H. *Nucl. Phys.* B378:95 (1992)
39. Teaney T. arXiv:nucl-th/0204023
40. Hirano T, Tsuda K. *Phys. Rev. C* 66:054905 (2002)
41. Kolb PF, Rapp R. *Phys. Rev. C* 67:044903 (2003)
42. Cooper F, Frye G. *Phys. Rev. D* 10:186 (1974)
43. Sollfrank J, Koch P, Heinz U. *Z. Phys. C* 52:593 (1991)
44. Eskola KJ et al. *Phys. Rev. C* 72:044904 (2005)
45. Adams J et al. [STAR Collaboration]. *Phys. Rev. Lett.* 91:172302 (2003)
46. Adler C et al. [STAR Collaboration]. *Phys. Rev. Lett.* 89:202301 (2002)
47. Adams J et al. [STAR Collaboration]. *Phys. Rev. Lett.* 92:112301 (2004)
48. Adler C et al. [STAR Collaboration]. *Phys. Rev. Lett.* 89:092301 (2002)
49. Adler SS et al. [PHENIX Collaboration]. *Phys. Rev. C* 69:034910 (2004)
50. Adcox K et al. [PHENIX Collaboration]. *Phys. Rev. Lett.* 88:022301 (2002)
51. Adcox K et al. [PHENIX Collaboration]. *Phys. Rev. Lett.* 88:242301 (2002)
52. Adcox K et al. [PHENIX Collaboration]. *Phys. Rev. Lett.* 89:092302 (2002)
53. Adler SS et al. [PHENIX Collaboration], *Phys. Rev. C* 69:034909 (2004)
54. Adler SS et al. [PHENIX Collaboration]. *Phys. Rev. Lett.* 91:072301 (2003)
55. Back BB et al. [PHOBOS Collaboration]. *Phys. Lett.* B578:297 (2004)
56. Back BB et al. [PHOBOS Collaboration]. arXiv:nucl-ex/0401006
57. Arsene I et al. [BRAHMS Collaboration]. *Phys. Rev. Lett.* 91:072305 (2003)
58. Bearden IG et al. [BRAHMS Collaboration]. *Phys. Rev. Lett.* 94:162301 (2005)
59. Bearden IG et al. [BRAHMS Collaboration]. *Phys. Rev. Lett.* 93:102301 (2004)
60. Hirano T, Gyulassy M. arXiv:nucl-th/0506049
61. Hirano T et al. arXiv:nucl-th/0511046
62. Eskola KJ, Honkanen H, Salgado CA, Wiedemann UA. *Nucl. Phys.* A747:511 (2005)

63. Fries RJ. *J. Phys. G* 30:S853 (2004); Hwa RC. *Eur. Phys. J. C* 43:233 (2005)
64. Voloshin S, Zhang Y. *Z. Phys. C* 70:665 (1996)
65. Kolb PF. *Phys. Rev. C* 68:031902 (2003)
66. Adams J et al. [STAR Collaboration]. *Phys. Rev. Lett.* 92:062301 (2004)
67. Poskanzer AM. *J. Phys. G* 30:S1225 (2004)
68. Molnar D, Huovinen P. *Phys. Rev. Lett.* 94:012302 (2005)
69. Siemens PJ, Rasmussen JO. *Phys. Rev. Lett.* 42:880 (1979)
70. Kolb PF, Sollfrank J, Heinz UW. *Phys. Rev. C* 62:054909 (2000)
71. Agakichiev G et al. [CERES/NA45 Collaboration]. *Phys. Rev. Lett.* 92:032301 (2004)
72. Heinz U, Kolb PF. *J. Phys. G* 30:S1229 (2004)
73. Teaney D, Lauret J, Shuryak EV. arXiv:nucl-th/0110037
74. Bass SA, Dumitru A. *Phys. Rev. C* 61:064909 (2000)
75. Nonaka C, Bass SA. arXiv:nucl-th/0510038
76. Miller M, Snellings R. arXiv:nucl-ex/0312008
77. Hama Y, Kodama T, Socolowski OJ. *Braz. J. Phys.* 35:24 (2005)
78. Adams J et al. [STAR Collaboration]. *Phys. Rev. C* 72:014904 (2005)
79. Adler SS et al. [PHENIX Collaboration]. *Phys. Rev. Lett.* 91:182301 (2003)
80. Gyulassy M, McLerran L. *Nucl. Phys. A* 750:30 (2005); Shuryak EV. *Nucl. Phys. A* 750:64 (2005); Heinz UW. arXiv:nucl-th/0512051
81. Teaney DA. *J. Phys. G* 30:S1247 (2004); Chaudhuri AK, Heinz UW. arXiv:nucl-th/0504022
82. Back BB et al. [PHOBOS Collaboration]. *Phys. Rev. Lett.* 89:222301 (2002)
83. Back BB et al. [PHOBOS Collaboration]. *Phys. Rev. C* 72:051901 (2005)
84. Staszal P. [BRAHMS Collaboration], arXiv:nucl-ex/0510061; Johnson EB. arXiv:nucl-ex/0601010
85. Adler C et al. [STAR Collaboration]. *Phys. Rev. C* 66:034904 (2002)
86. Back BB et al. [PHOBOS Collaboration]. *Phys. Rev. Lett.* 91:052303 (2003)
87. Hirano T. *Phys. Rev. C* 65:011901 (2002)
88. Hanbury Brown R, Twiss RQ. *Nature* 178:1046 (1956)
89. Wiedemann UA, Heinz UW. *Phys. Rep.* 319:145 (1999)
90. Lisa M, Pratt S, Soltz R, Wiedemann UA. *Annu. Rev. Nucl. Part. Sci.* 55:357 (2005)
91. Tomasik B, Wiedemann UA. in *Quark-Gluon Plasma 3*, ed. RC Hwa, XN Wang. Singapore: World Scientific (2004) [arXiv:hep-ph/0210250]
92. Kolb PF, Heinz U. in *Quark-Gluon Plasma 3*, ed. RC Hwa, XN Wang. Singapore: World Scientific (2004) [arXiv:nucl-th/0305084]

93. Rischke DH, Gyulassy M. *Nucl. Phys.* A608:479 (1996)
94. Soff S, Bass SA, Dumitru A. *Phys. Rev. Lett.* 86:3981 (2001); Soff S. arXiv:hep-ph/0202240
95. Adams J. et al. [STAR Collaboration]. *Phys. Rev. C* 71:044906 (2005)
96. Adler SS et al. [PHENIX Collaboration]. *Phys. Rev. Lett.* 93:152302 (2004)
97. Morita K, Muroya S, Nonaka C, Hirano T. *Phys. Rev. C* 66:054904 (2002)
98. Zschesche D, Schramm S, Stocker H, Greiner W. *Phys. Rev. C* 65:064902 (2002)
99. Grassi F, Hama Y, Padula SS, Socolowski OJ. *Phys. Rev. C* 62:044904 (2000); Sinyukov YM, Akkelin SV, Hama Y. *Phys. Rev. Lett.* 89:052301 (2002)
100. Dumitru A. arXiv:nucl-th/0206011
101. Arleo F et al. *CERN Yellow Report on Hard Probes in Heavy Ion Collisions at the LHC*, CERN, Geneva (2003) [arXiv:hep-ph/0311131]
102. Kapusta JI, Lichard P, Seibert D. *Phys. Rev. D* 44:2774 (1991). Erratum. *Phys. Rev. D* 47:4171 (1993)
103. Baier R, Nakkagawa H, Niegawa A, Redlich K. *Z. Phys. C* 53:433 (1992)
104. Aurenche P, Gelis F, Kobes R, Petitgirard E. *Z. Phys. C* 75:315 (1997); Aurenche P, Gelis F, Kobes R, Zaraket H. *Phys. Rev. D* 58:085003 (1998); Aurenche P, Gelis F, Zaraket H. *JHEP* 0205:043 (2002)
105. Steffen FD, Thoma MH. *Phys. Lett.* B510:98 (2001)
106. Arnold P, Moore GD, Yaffe LG. *JHEP* 0111:057 (2001)
107. Arnold P, Moore GD, Yaffe LG. *JHEP* 0112:009 (2001)
108. Gale C, Haglin KL. in *Quark-Gluon Plasma 3*, ed. RC Hwa, XN Wang. Singapore: World Scientific (2004) [arXiv:hep-ph/0306098]
109. Xiong L, Shuryak E, Brown GE. *Phys. Rev. D* 46:3798 (1992)
110. Song C. *Phys. Rev. C* 47:2861 (1993)
111. Gao S, Gale C. *Phys. Rev. C* 57:254 (1998)
112. Turbide S, Rapp R, Gale C. *Phys. Rev. C* 69:014903 (2004)
113. Haglin KL. *J. Phys. G* 30:L27 (2004)
114. Wong CY. *Introduction to Heavy Ion Collisions*. Singapore: World Scientific (1994)
115. Cleymans J, Fingberg J, Redlich K. *Phys. Rev. D* 35:2153 (1987)
116. Braaten F, Pisarski RD, Yuan TC. *Phys. Rev. Lett.* 64:2242 (1990)
117. Altherr T, Ruuskanen PV. *Nucl. Phys.* B380:377 (1992)
118. Aurenche P, Gelis F, Moore GD, Zaraket H. *JHEP* 0212:006 (2002)
119. Karsch F, et al. *Phys. Lett.* B530:147 (2002)

120. Agakishiev G et al. [CERES/NA45 Collaboration]. *Phys. Lett.* B422:405 (1998); Lenkeit B et al. [CERES-Collaboration]. *Nucl. Phys.* A661:23 (1999); Marin A [CERES Collaboration]. *J. Phys. G* 30:S709 (2004); Agakichiev G et al. [CERES Collaboration]. *Eur. Phys. J. C* 41:475 (2005)
121. Rapp R, Wambach J. *Adv. Nucl. Phys.* 25:1 (2000)
122. Gale C, P. Lichard P. *Phys. Rev. D* 49:3338 (1994); Lichard P. *Phys. Rev. D* 49:5812 (1994)
123. Rapp R, Chanfray G, Wambach J. *Nucl. Phys.* A617:472 (1997); Rapp R. *Phys. Rev. C* 63:054907 (2001)
124. Eletsy VL, Belkacem M, Ellis PJ, Kapusta JI. *Phys. Rev. C* 64:035202 (2001)
125. Huovinen P, Belkacem M, Ellis PJ, Kapusta JI. *Phys. Rev. C* 66:014903 (2002)
126. Brown GE, Rho M. *Phys. Rep.* 269:333 (1996)
127. Aggarwal MM et al. [WA98 Collaboration]. *Phys. Rev. Lett.* 85:3595 (2000); arXiv:nucl-ex/0006007
128. Srivastava DK, Sinha B. *Phys. Rev. C* 64:034902 (2001)
129. Alam J et al. *Phys. Rev. C* 63:021901 (2001); Alam J, Roy P, Sarkar S, Sinha B. *Phys. Rev. C* 67:054901 (2003)
130. Peressounko DY, Pokrovsky YE. hep-ph/0009025
131. Chaudhuri AK. *J. Phys. G* 29:235 (2003)
132. Huovinen P, Ruuskanen PV, Räsänen SS. *Phys. Lett.* B535:109 (2002)
133. Huovinen P, Ruuskanen PV, Sollfrank J. *Nucl. Phys.* A650:227 (1999)
134. Wong C, Wang H. *Phys. Rev. C* 58:376 (1998)
135. Bathe S [PHENIX Collaboration]. arXiv:nucl-ex/0511042
136. Räsänen SS. *Nucl. Phys.* A715:717 (2003)
137. Gelis F, Niemi H, Ruuskanen PV, Räsänen SS. *J. Phys. G* 30:S1031 (2004)
138. d'Enterria D, Peressounko D. arXiv:nucl-th/0503054
139. Hammon N, Dumitru A, Stoecker H, Greiner W. *Phys. Rev. C* 57:3292 (1998)
140. Srivastava DK, *Eur. Phys. J. C* 10:487 (1999). Erratum. *Eur. Phys. J. C* 20:399 (2001)
141. Peressounko DY, Pokrovsky YE. *Nucl. Phys.* A669:196 (2000)
142. Fries RJ, Muller B, Srivastava DK. *Phys. Rev. Lett.* 90:132301 (2003)
143. Eskola KJ, Kajantie K, Ruuskanen PV. *Eur. Phys. J. C* 1:627 (1998)
144. Peitzmann T, Thoma MH. *Phys. Rep.* 364:175 (2002)
145. Shuryak EV. *Phys. Rev. Lett.* 68:3270 (1992)
146. Mustafa MG, Thoma MH. *Phys. Rev. C* 62:014902 (2000). Erratum. *Phys. Rev. C* 63:069902 (2001)

147. Agakishiev G et al. [CERES Collaboration]. *Phys. Rev. Lett.* 75:1272 (1995)
148. Abreu MC et al. [NA38 and NA50 Collaborations]. *Eur. Phys. J. C* 14:443 (2000)
149. Srivastava DK, Sinha B, Gale C. *Phys. Rev. C* 53:567 (1996)
150. Hung CM, Shuryak EV. *Phys. Rev. C* 56:453 (1997)
151. Huovinen P, Prakash M. *Phys. Lett.* B450:15 (1999)
152. Kvasnikova I, Gale C, Srivastava DK. *Phys. Rev. C* 65:064903 (2002)
153. Miskowiec D [CERES Collaboration]. arXiv:nucl-ex/0511010
154. Damjanovic S et al. [NA60 Collaboration]. arXiv:nucl-ex/0510044
155. Brown GE, Rho M. arXiv:nucl-th/0509001
156. Shuryak EV. *Phys. Lett.* B78:150 (1978); Kajantie K, Kapusta JI, McLerran LD, Mekjian A. *Phys. Rev. D* 34:2746 (1986)
157. Rapp R. *J. Phys. G* 31:S217 (2005)
158. Shuryak EV. *Phys. Rev. C* 55:961 (1997)
159. Turbide S, Gale C, Srivastava DK, Fries RJ. arXiv:hep-ph/0601042
160. Toia A [PHENIX Collaboration]. arXiv:nucl-ex/0510006
161. Ravinovich I et al. arXiv:nucl-ex/0510024